CrossMark
click for updates

View Article Online
View Journal

JAAS

Accepted Manuscript

This article can be cited before page numbers have been issued, to do this please use: C. Fàbrega, D. Parcerisa, J. M. Rossell, A. Gurenko and C. Franke, *J. Anal. At. Spectrom.*, 2017, DOI: 10.1039/C6JA00397D.

This is an Accepted Manuscript, which has been through the Royal Society of Chemistry peer review process and has been accepted for publication.

Accepted Manuscripts are published online shortly after acceptance, before technical editing, formatting and proof reading. Using this free service, authors can make their results available to the community, in citable form, before we publish the edited article. We will replace this Accepted Manuscript with the edited and formatted Advance Article as soon as it is available.

You can find more information about Accepted Manuscripts in the author guidelines.

Please note that technical editing may introduce minor changes to the text and/or graphics, which may alter content. The journal's standard Terms & Conditions and the ethical guidelines, outlined in our author and reviewer resource centre, still apply. In no event shall the Royal Society of Chemistry be held responsible for any errors or omissions in this Accepted Manuscript or any consequences arising from the use of any information it contains.

ROYAL SOCIETY OF CHEMISTRY

rsc.li/jaas

View Article Online
DOI: 10.1039/C6JA00397D

JAAS

PAPER

Predicting instrumental mass fractionation (IMF) of stable isotope SIMS analyses by response surface methodology (RSM)†

Received 00th January 20xx,
Accepted 00th January 20xx

DOI: 10.1039/x0xx00000x

www.rsc.org/

C. Fàbrega[a], D. Parcerisa[a], J. M. Rossell[b], A. Gurenko[c], C. Franke[d]

Instrumental mass fractionation (IMF) of isotopic SIMS analyses (Cameca 1280HR, CRPG Nancy) was predicted by response surface methodology (RSM) for $^{18}O/^{16}O$ determinations of plagioclase, K-feldspar, and quartz. The three predictive response surface models combined instrumental and compositional inputs. The instrumental parameters were: (i) X and Y stage position, (ii) the values of LT1DefX and LT1DefY electrostatic deflectors, (iii) chamber pressure and, (iv) primary-ion beam intensity. The compositional inputs included: (i) anorthite content (An%) for the plagioclase model and, (ii) orthoclase (Or%) and barium (BaO%) contents for the K-feldspar model. The three models reached high predictive powers. The coefficients R^2 and prediction-R^2 were, respectively, 90.47% and 86.74% for plagioclase, 87.56% and 83.17% for K-feldspar, and 94.29% and 91.59% for quartz. The results show that RSM can be confidently applied to IMF prediction in stable isotope SIMS analyses by the use of instrumental and compositional variables.

1 Introduction

Determination and correction of IMF is one of the key steps to obtain reliable results in stable isotope SIMS measurements of mineral samples. The instrumental mass bias occurs during several phases of SIMS analyses, e.g. sputtering, ionization, extraction, secondary beam transmission and detection,[1] which depend on the ion microprobe operating conditions.[2,3] In addition, IMF is strongly influenced by the major elements composition of the mineral.[4] This has focused an intense research on the instrumental and compositional factors influencing IMF, the so-called "matrix effect". Eiler *et al.* reported correlations of IMF with the ion sputtering rate and the atomic mass unit of the network-modifying cations in $^{18}O/^{16}O$ of target silicates, phosphates and glasses.[5] Riciputi *et al.* showed a correlation of IMF with chemical composition, the intensity of primary-ion beam, amount of the implanted $^{133}Cs^+$ and kinetic energy of the sputtered ions in $^{34}S/^{32}S$, $^{18}O/^{16}O$ and $^{13}C/^{12}C$ analyses of sulfides, silicates, oxides, and carbonates.[1] Gurenko *et al*. correlated the IMF of $^{18}O/^{16}O$ analyses on volcanic glasses and pyroxenes with compositional parameters.[6] Hauri *et al.* obtained linear regressions of IMF vs. chemical, instrumental, and physical parameters in D/H analyses of volcanic glasses.[7] Vielzeuf *et al.* proposed a mathematical script for bias prediction of $^{18}O/^{16}O$ analyses as a function of garnet composition using Matlab (The MathWorks, Inc.).[8] Kita *et al.* reported the influence of X-Y mount position and sample topography on IMF using $^{18}O/^{16}O$ zircon analyses.[9] Page *et al.* fitted linear regressions of IMF versus the composition and molar volume in $^{18}O/^{16}O$ analyses of 25 garnet standards.[10] Rollion-Bard and Marin-Carbonne correlated IMF with Mg, Fe and Mn content in $^{18}O/^{16}O$ measurements of the calcite-siderite-magnesite solid-solution series.[11] Hartley *et al.* correlated the IMF of $^{18}O/^{16}O$ glass standards analyses and the chemical composition, physical properties and instrumental setting.[12] Slodzian *et al.* correlated the IMF with the chemical composition, the atomic concentration of implanted Cs and the sputtering yield in $^{29}Si/^{28}Si$ analyses of olivine and quartz.[13] Ickert and Stern correlated IMF with Ca content in garnet $^{18}O/^{16}O$ analyses.[14] Śliwiński *et al.* correlated the Fe content with bias variation in $^{18}O/^{16}O$ and $^{13}C/^{12}C$ analyses of the dolomite-ankerite solid solution series using the Hill's equation for nonlinear effects.[15,16]

Introduced by Box and Wilson, RSM has been applied to build up multivariate statistical models in a wide variety of industrial, engineering and experimental processes.[17] Successful RSM applications can be found in, e.g., Riley, Legtenberg, Chen *et al.*, Hung *et al.*, Angellier *et al.*, Noordin *et al.*, Bas and Boyaci, Bezerra *et al.*, Habib, Tarley *et al.*, Ali *et al.*, Azhari *et al.* and Mohamed *et al*.[18–30] In addition, the mathematical and statistical aspects of RSM and related experimental techniques are covered in e.g., Box, Box, and

[a] Departament d'Enginyeria Minera, Industrial i TIC, Escola Politècnica Superior d'Enginyeria de Manresa (UPC – Campus Manresa), Av. Bases de Manresa, 61-73, 08242, Manresa. E-mail: dparcerisa@epsem.upc.edu
[b] Departament de Matemàtiques, Escola Politècnica Superior d'Enginyeria de Manresa (UPC – Campus Manresa), Av. Bases de Manresa, 61-73, 08242, Manresa.
[c] Centre de Recherches Pétrographiques et Géochimiques, UMR 7358, Université de Lorraine, 15 rue Notre-Dame des Pauvres, BP 20, 54501 Vandoeuvre-lès-Nancy, France.
[d] MINES ParisTech, PSL Research University, Center of Geosciences, 35 rue St. Honoré, 77305, Fontainebleau, Cedex, France.

† Electronic Supplementary Information (ESI) available: S1. CL and BSE STANDARD images; S2. SIMS, EPMA and Fluorination data; S3. Response Surface Models; and S4. Response Surface Model construction. See DOI: 10.1039/x0xx00000x

This journal is © The Royal Society of Chemistry 20xx

Please do not adjust margins

Published on 10 February 2017. Downloaded by Universitat Politècnica de Catalunya on 14/02/2017 11:31:26.

Journal of Analytical Atomic Spectrometry Accepted Manuscript

View Article Online
DOI: 10.1039/C6JA00397D

Published on 10 February 2017. Downloaded by University Politecnica de Catalunya on 14/02/2017 11:31:26.

Draper, Carley *et al.*, del Castillo, Myers *et al.*, Khuri and Mukhopadhyay and Barton.[31–37]

Simultaneously, the statistical prediction models have been recognized as powerful tools for e.g., exploring the underlying causal relationships below the datasets, building and/or assessing new knowledge and improving previous models.[38] While explanatory statistical modelling is based on the causal relationships among previous theoretical constructions, the predictive statistical modelling works on associations of measurable variables. The discrimination of both approaches as different but complementary tools has been strongly emphasized by e.g., Dowe *et al.*, Hitchcock and Sober and Konishi and Kitagama.[39–41] Usually, statistical models present a mix of predictive and explanatory power so that, to increase the predictive strength and reduce the sampling variance it is necessary to partly sacrifice the theoretical accuracy.[42] Shmueli demonstrated that the predictions of a "wrong" model present lower prediction error than a more "true" model, especially in situations dealing with e.g., low quality data, small populations of observations or highly correlated variables.[38]

The main purpose of this study was to construct and develop three predictive response surface models to IMF correction of $^{18}O/^{16}O$ SIMS analyses of plagioclase, K-feldspar, and quartz. The second goal of the study was the application of these three response surface models to correct, respectively, IMF of igneous plagioclase, K-feldspar and quartz $^{18}O/^{16}O$ SIMS analyses of Variscan granite samples from NE Spain carried out during the same session. The use of RSM in this study permitted to deal with:

i. Large distances among the standards and the target samples. Rock samples covered an area in the mount about 20-25 mm^2 in order preserve most of the textural features, so the distance from the standards to the target points was for practical reasons in many cases about thousands of microns.
ii. The electrostatic deflectors of the standards and the samples presented significant different values.
iii. Minor punctual instabilities of the chamber pressure appeared during the session.
iv. Different from the usual standard bracketing correction method, which assigns the same value of averaged IMF to all SIMS analyses interpolated within each standard-bracket, the RSM permits the prediction of a single and unique IMF value for each SIMS analysis.
v. The observations from the initial Exploratory Data Analysis (EDA) and from the final RSM models permitted to explore the "causal" relationships among the instrumental and compositional variables and IMF of stable isotope SIMS analyses, the so-called "matrix effect".

2 RSM

RSM is a combination of mathematical and statistical tools designed to build up multiple variables polynomial models.[32] It has proven particularly useful for the development and optimization of processes and products and for characterizing the behavior of a predicted variable (i.e. the response) within a given operational region of several input variables.[35] RSM is especially valuable to obtain an "approximation" function of the "actual" unknown function f of the underlying phenomenon. The approach is usually carried out by a second order polynomial containing linear, interaction and squared terms, by Eq. (1):

$$y = \beta_0 + \sum_{i=1}^{n} \beta_i X_i + \sum_{j=2}^{n} \sum_{i<j} \beta_{ij} X_i X_j + \sum_{i=1}^{n} \beta_{ii} X_i^2 + \varepsilon \qquad (1)$$

The variable y being the expected or predicted response, $X_i, i = 1,2,\dots,\mathrm{n}$, the input variables, β_0 the constant term, $\beta_i, \beta_{ij}, \beta_{ii}, i, j = 1,2,\dots,n$, the equation coefficients and ε the standard error of the prediction, which is assumed to have zero mean.

The adjusting of the polynomial to data is carried out by the least squares method (*LSM*), by minimizing the sum of squared residuals. The statistical significance of the model is evaluated by the *ANOVA* test (analysis of the variance). The statistical significance (*p-value*) applied to accept the terms in the model is generally *p-value* ≤ 0.05 (i.e. 95% confidence level). Simultaneously, multicollinearity must be properly controlled to avoid highly correlated terms in the model, usually by the variance inflation factor (*VIF*). Generally, the terms showing *VIF* > 10 are considered to suffer high multicollinearity and it is recommended to exclude them from the model.

The selection of the model terms is habitually carried out by a sequential stepwise backward elimination process.[33,35] In each step, the no significant term displaying the highest *p-value* is eliminated and then the model is refitted again. The procedure sequentially repeats until, ideally most of the remaining model terms display proper levels of significance (*p-value* ≤ 0.05) and multicollinearity (*VIF* ≤ 10). To reach this goal, the observations used to fit the model must properly cover the operational region of the input variables. To fit a hierarchical model, the non-significant linear terms participating in significant interaction or squared terms must be preserved in the model. The stepwise backward elimination sequence can lead to slightly different final models that, depending on the desired accuracy, can be equally adequate for a given applied work. It is recommended to develop the model in teamwork, running the backward elimination process by separate investigators and compare among independently fitted models.

The adequacy of the fitted model is evaluated by the standard error of the regression (*S*), the prediction error sum of squares (*PRESS*), the determination coefficients R^2, adjusted-R^2 and prediction-R^2, the analysis of residuals, the diagnostic of influence points (*Leverage*, *Cook's distance*) and the adequate precision (A*P*).

The standard error of the regression (*S*) calculates the average distance between the predicted values and the actual observations. *S* is calculated in the natural units of the response, so provides a rapid and intuitive measure of the model precision. Thus, when $y_i, i = 1,2,\dots,\mathrm{n}$, the actual

This journal is © The Royal Society of Chemistry 20xx

Journal of Analytical Atomic Spectrometry Accepted Manuscript

Please do not adjust margins

View Article Online
DOI: 10.1039/C6JA00397D

Published on 10 February 2017. Downloaded by Universitat Politecnica de Catalunya on 14/02/2017 11:31:26.

values, $\hat{y}_i$ the model predicted values of the same observations and n the number of observations, the standard error of the regression (*S*) can be written as Eq. (2):

$$S = \sqrt{\frac{\sum_{i=1}^{n}(y_i - \hat{y}_i)^2}{n}} \quad (2)$$

The prediction error sum of squares (*PRESS*) calculates the sum of squares of the prediction errors of the model points. The prediction error of a given point *i* is the distance between the actual and predicted value, calculated by the prediction model refitted without this *i* observation. So, when $y_i, i = 1,2,\dots,n$, the real observations and $\hat{y}_{i,-i}$ the predictions of the model refitted without using the *i* observation in each case, *PRESS* can be expressed as Eq. (3):

$$PRESS = \sum_{i=1}^{n}\left(y_i - \hat{y}_{i,-i}\right)^2 \quad (3)$$

The coefficient of determination R^2 (0-100%) estimates the amount of variability of the observations that is explained by the model. Thus, when $y_i, i = 1,2,\dots,n$ the actual observations of a sample, $\bar{y}$ their mean and $\hat{y}_i$ the model predictions of the same observations, the total sum of squares (SS_{tot}) is defined as Eq. (4):

$$SS_{tot} = \sum_{i=1}^{n}(y_i - \bar{y})^2 \quad (4)$$

The residual sum of squares (SS_{res}) by Eq. (5):

$$SS_{res} = \sum_{i=1}^{n}(y_i - \hat{y}_i)^2 \quad (5)$$

Then, the coefficient of determination R^2 is calculated by Eq. (6):

$$R^2 = 1 - \frac{SS_{res}}{SS_{tot}} \quad (6)$$

The *adjusted*-R^2 corrects for the number of terms included in the model and it is always lower than R^2. It is especially useful for comparisons among models with a different number of terms. Thus, being *n* the number of observations of the dataset and *p* the number of input variables included in the model (without the constant term), the *adjusted*-R^2 is calculated as Eq. (7):

$$Adj.R^2 = 1 - (1 - R^2)\frac{n-1}{n-p} \quad (7)$$

The *prediction*-R^2 estimates the capability of the model to explain the variability of new observations. It is always lower than R^2 and *adjusted*-R^2, calculated by Eq. (8):

$$Pred.R^2 = 1 - \frac{PRESS}{SS_{tot}} \quad (8)$$

Importantly, the values of R^2, *adjusted*-R^2, and *prediction*-R^2 should be as high and similar as possible. This indicates that the model has a satisfactory capacity to explain the experimental data and a proper predictive capability for new observations. When the model presents an excess of terms, the *adjusted*-R^2 is much lower than R^2. In addition, when the model has an excessive number of variables with regard to the number of observations used to fit the model (i.e. an over-fitted model), the *prediction*-R^2 is much lower than the R^2 and *adjusted*-R^2.

The residuals have a notable role in assessing the adequacy of the model. The residual analysis must be done on the observations listed in chronological order. Residuals can be expressed as $r_i = (y_i - \hat{y}_i), i = 1,2,\dots,n$, where y_i is the actual and $\hat{y}_i$ is the predicted value of the *i* observation. It is recommended to use a standardized population of residuals with μ≈ 0 and σ≈ 1, dividing each residual by the standard deviation of the residual's population. Properly, the standardized residuals should remain in the interval (-3, 3), but ultimately this limit depends on the experience of the investigator and on the goal of the study. The standardized residuals out of this interval are potential outliers and must be re-examined, as they could indicate, e.g., sampling errors or a poor fitting of the model in that region of the variables. Usually, standardized residuals are graphically analysed. Thus, the cumulated probability distribution function and the histogram should approach a normal distribution. In addition, the plots of residuals vs. response, the time series (order of analyses) and the predictor variables should display random distributions. Importantly, the observation of trends in the residual plots indicates that significant variables on the response are not included in the model.

The influential observations (points) must be detected to avoid the fitting of biased models. The potential influence of a given point can be evaluated by the leverage (*Hi*) and the Cook's distance (D_i). The leverage indicates when a model point has remote or extreme values of the input variables. Generally, *Hi* is recommended to be $Hi \leq 2p/n$, were *p* is the number of predictor terms of the model including the constant, and *n* the number of observations used to fit the model. The detection of a high *Hi* value is not negative itself, and the influence of that point should be further evaluated by the Cook's distance (D_i). D_i estimates how the model regression coefficients change when a given point *i* is omitted from the model and this it is refitted again. Those points with relatively large values of D_i respect to the rest of the population of points or with $D_i \geq 0.5$ are potentially influential observations and should be carefully re-examined (Cook).[43] If high Cook's distances are detected, it is recommended to exclude the affected points and re-fit the model again to compare the changes. The capacity of the influential observations to deviate the fitted model can be strong, so the detection of influential observations is a critical step to avoid biased models.

The adequate precision (*AP*) calculates the ratio between the range of values of the response and the averaged standard error of the model predictions, i.e. the signal out of noise: $AP = (y_{max} - y_{min})/average\ SE_{prediction}$. As a rule of thumb, AP ≥ 4 is recommended.

Journal of Analytical Atomic Spectrometry Accepted Manuscript

Please do not adjust margins

View Article Online
DOI: 10.1039/C6JA00397D

Published on 10 February 2017. Downloaded by Universitat Politècnica de Catalunya on 14/02/2017 11:31:26.

When the adequate response Surface model is finished, the behavior of the response through the model is usually visualized by 3D surface or contour plots of the response versus pairs of variables, while keeping fixed the rest of the input variables.

3 Analytical process

3.1 Selection and characterization of standards

The SIMS points used to construct the three response surface models of this study were analyzed on internal standards, selected and characterized from natural specimens of plagioclase, K-feldspar, and quartz. In a first step, bulk fragments of about 30 potential specimens were examined using scanning electron microscopy and energy dispersive spectroscopy (SEM-EDS) at the Escola Politècnica Superior d'Enginyeria de Manresa of the Universitat Politècnica de Catalunya (Spain). The specimens presenting no visible or minimal visual heterogeneities in BSE mode and virtually uniform composition in EDS were prepared as thin sections (30 µm-thick) with metallographic polishing for further petrographic and compositional analyses.

These selected specimens were texturally and compositionally analyzed using the following techniques:

i. Petrographic analyses were performed using a Nikon Eclipse E400 petrographic microscope at the Escola Politècnica Superior d'Enginyeria de Manresa of the Universitat Politècnica de Catalunya (Spain).

ii. SEM-EDS analyses were carried out using a Hitachi TM-1000 operating at 15 Kv at the Escola Politècnica Superior d'Enginyeria de Manresa of the Universitat Politècnica de Catalunya (Spain). Backscatter diffracted electron (BSE) imaging is especially useful for the detection of perthites and antiperthites in K-feldspar and plagioclase, respectively.

iii. Optical cathodoluminescence (CL) observations were performed under a Technosyn Cold Cathodoluminescence model 8200 MKII CL, equipped with a Nikon Coolpix 4500 digital camera at the Facultat de Geologia of the Universitat de Barcelona (Spain). CL working conditions went from 15 to 18 kV gun potential and 150 to 350 µA beam current. Afterwards, the quality of the CL pictures was improved by adjusting the colour histograms of the images following Witkowski *et al.*[44] Importantly, optical-CL permits the detection of textural features in minerals indicative of potential geochemical heterogeneities where BSE images do not show visible contrast because the major element composition does not significantly change, e.g., recrystallization, internal zoning, micro-cracks cement or overgrowths. Specimens presenting large areas with important cathodoluminescence heterogeneities should not be used as standards.

iv. The chemical composition of the standards was determined by EPMA under a JEOL JXA-8230 operating at 20 Kv and equipped with five dispersive wavelength spectrometers (WDS), at the Centres Científics i Tecnològics of the Universitat de Barcelona (Spain). The EPMA analyses were distributed in several grains of each specimen to check that chemical composition was homogeneous at millimeter scale.

v. Finally, the $^{18}O/^{16}O$ isotope ratios of plagioclase, K-feldspar and quartz specimens selected as adequate standards were determined by CO_2-laser fluorination at the Laboratorio General de Análisis de Isótopos Estables of the Universidad de Salamanca (Spain). About 4-6 mg of material was carefully extracted from each standard using a tungsten 0.65 mm diameter dental drill with the aid of a binocular scope. After extraction, the sampling craters were analyzed by SEM-EDS to check that the drilled material was virtually homogeneous.

3.2 Textural and compositional features of the standards

The eight plagioclase, two K-feldspar, and one quartz internal standards used in this study were selected to develop a response surface model for each mineral group (Table 1). The plagioclase specimens covered most of the albite-anorthite solid solution series and the K-feldspar standards represented the K-feldspar compositional end-member. The cathodoluminescence, BSE images, and EPMA analyses of the standards are included in the electronic supplementary information (S1 and S2)†. The characteristics of the standards used in this study are as follow:

Table 1 Fluorination $\delta^{18}O_{VSMOW}$ results for plagioclase, K-feldspar and quartz standards

Mineral	Plagioclase							
	Albite	Albite	Oligoclase	Andesine	Labradorite	Labradorite	Bytownite	Anorthite
Ref.	Gstd0001	Gstd0002	Gstd0003	Gstd0004	Gstd0005	Gstd0006	Gstd0008	Gstd0009
n	3	3	2	2	3	3	2	2
$\delta^{18}O‰\pm1\sigma$	9.73±0.15	12.36±0.15	8.20±0.05	7.50±0.23	7.50±0.26	7.33±0.15	6.85±0.03	7.05±0.20
$^{18}O/^{16}O$	0.002024717	0.00203000	0.00202164	0.00202024	0.00202024	0.00201990	0.00201894	0.00201934

Mineral	K-feldspar		Quartz
	Adularia	Microcline	
Ref.	Gstd0010	Gstd0011	Gstd0012
n	2	4	3
$\delta^{18}O‰\pm1\sigma$	9.30±0.05	9.23±0.21	9.36±0.10
$^{18}O/^{16}O$	0.00202385	0.00202370	0.00202398

This journal is © The Royal Society of Chemistry 20xx

Journal of Analytical Atomic Spectrometry Accepted Manuscript

View Article Online
DOI: 10.1039/C6JA00397D

Published on 10 February 2017. Downloaded by Universitat Politecnica de Catalunya on 14/02/2017 11:31:26.

i. *Gstd0001*: 2.5 cm-sized, translucent, labradorescent, brunet albite crystal from Hybla, Ontario, Canada. CL showed dull brown luminescence. The average feldspar composition was $Ab_{91}An_7Or_2$, falling in the lower part of the albite range. The reference $^{18}O/^{16}O$ ratio was 0.002024717 ($^{18}\delta O_{VSMOW}$= 9.7‰).

ii. *Gstd0002*: 6 cm-sized, translucent, white albite specimen from Bancroft, Ontario, Canada. CL presented pale-blue-red colors. The average feldspar composition was $Ab_{93}An_6Or_1$, in the lower half of the albite range. The fluorination $^{18}O/^{16}O$ ratio was 0.002029998 ($^{18}\delta O_{VSMOW}$ = 12.4‰).

iii. *Gstd0003*: 5 cm-sized, translucent, white oligoclase specimen from Madawaska, Ontario, Canada. CL exhibited bright green luminescence. The average feldspar composition was $Ab_{76}An_{22}Or_2$, in the center of the oligoclase range. The bulk $^{18}O/^{16}O$ ratio was 0.002021643($^{18}\delta O_{VSMOW}$ = 8.2‰).

iv. *Gstd0004*: 1.2 cm-sized, gemstone quality, translucent, violet andesine/labradorite crystal from Congo. CL was intense purple. The average feldspar composition was $Ab_{48}An_{50}Or_2$. The reference $^{18}O/^{16}O$ ratio was 0.002020239 ($^{18}\delta O_{VSMOW}$ = 7.5‰).

v. *Gstd0005*: 4 cm-sized, labradorescent, dark labradorite specimen from Labrador, Canada. CL exhibited pale green luminescence. The mean feldspar composition was $Ab_{44}An_{54}Or_2$, in the middle of labradorite range composition. The fluorination $^{18}O/^{16}O$ ratio was 0.002020239 ($^{18}\delta O_{VSMOW}$ = 7.5‰).

vi. *Gstd0006*: 1 cm-sized, almost black, labradorescent labradorite crystal from Grass Valley, California, USA. CL was homogeneous dull grey. The average feldspar composition fell in the lower half of the labradorite range, being $Ab_{37}An_{62}Or_1$. The bulk $^{18}O/^{16}O$ ratio was 0.002019905 ($^{18}\delta O_{VSMOW}$ = 7.3‰).

vii. *Gstd0008*: 0.2-0.5 cm-sized, translucent, white bytownite fragments. CL displayed homogeneous, dull grey luminescence. The mean feldspar composition was $Ab_{23}An_{76}Or_1$, in the upper part of the bytownite range. The fluorination $^{18}O/^{16}O$ ratio was 0.002018936 ($^{18}\delta O_{VSMOW}$ = 6.9‰).

viii. *Gstd0009*: 2 cm-sized, translucent white anorthite crystal from Miyake Island, Japan. CL was homogeneous, pale green-brown. Feldspar composition was Ab_4An_{96}, falling in the lower part of the anorthite range. The reference $^{18}O/^{16}O$ ratio was 0.0020193367 ($^{18}\delta O_{VSMOW}$ = 7.1‰).

ix. *Gstd0010*: 3 cm-sized, translucent, orthoclase crystal from Grisons, Switzerland. CL exhibited dull blue luminescence. The average feldspar composition was $Ab_{11}Or_{89}$. The bulk $^{18}O/^{16}O$ ratio was 0.00202384836 ($^{18}\delta O_{VSMOW}$ = 9.3‰).

x. *Gstd0011*: 8 cm-sized, translucent, pink microcline specimen from Parry Sound, Ontario, Canada. CL was bright blue. Under BSE imaging showed crypto-perthites (< 5%).The averaged composition was Ab_7Or_{93}. The fluorination $^{18}O/^{16}O$ ratio was 0.00202369797 ($^{18}\delta O_{VSMOW}$ = 9.2‰).

xi. *Gstd0012*: 5 cm-sized, transparent, quartz crystal from Pazolastok, Oberalp, Switzerland. CL showed homogeneous dark luminescence. The composition was 99.9% SiO_2. The reference $^{18}O/^{16}O$ ratio was 0.00202398204 ($^{18}\delta O_{VSMOW}$ = 9.4‰).

The plagioclase, K-feldspar, and quartz standards used in this study are deposited in the Museu de Geologia Valentí Masachs of the Universitat Politècnica de Catalunya (Manresa, Spain) with the same reference labels.

3.3 Sample preparation for SIMS

Fragments about 3-5 mm of the plagioclase, K-feldspar, and quartz standards were cut off by a hand-manipulated 22 mm diameter / 0.6 mm thickness diamond wheel with the aid of a binocular scope. The portions were included in 25 mm diameter epoxy resin cylindrical mounts and the target surface was finished with a metallographic polishing. The surface roughness was checked under a digital profilometer Leica DCM 3D at the Servei de Microscopia of the Universitat Autònoma de Barcelona (Spain). The roughness values were below 1 µm, achieving the recommendations of Kita *et al.* to avoid topography effects on IMF.[9] Afterwards, the specimens included in the mounts were imaged by optical cathodoluminescence (CL) and SEM. These pictures were used to select suitable places for the $^{18}O/^{16}O$ isotope analysis in the grains during the SIMS session. The different positions of the standards in the mounts present from the central area virtually free of significant X-Y effects on IMF (i.e. 10-12 mm diameter) to extreme external positions (i.e. 20-22 mm diameter from the center) affected by X-Y effects.[9] Representative images of several standards mounts are included in the electronic supplementary information S1†.

3.4 $^{18}O/^{16}O$ SIMS measurements

The $^{18}O/^{16}O$ SIMS analyses were carried out using a Cameca IMS 1280HR at the Centre de Recherches Pétrographiques et Géochimiques, the Centre National de la Recherche Scientifique (Nancy, France). Measurements were carried out in one session from 22nd to 25th July 2014 under stable weather conditions. The sample surface was gold coated and bombarded by a $^{133}Cs+$ 5-6 nA primary beam in chamber pressure conditions about 10^{-9}Torr. The positive charge of the sample surface was compensated by a normal incident electron flood. Sputtered ions were accelerated to the secondary column by a -10 Kv potential. The secondary ion beam was automatically centered onto the field departures by the electrostatic deflectors LT1DefX and LT1DefY. The two oxygen isotopes ^{16}O and ^{18}O were simultaneously collected by two Faraday cups (FC). Each analysis included 30 cycles, with a total time about 4 minutes, including the 60 s pre-sputtering time.

During the SIMS session, the groups of analyses of plagioclase, K-feldspar, and quartz standards were sequentially alternated (Fig. 1) and intercalated with analyses of rock samples (not included in this study).

Journal of Analytical Atomic Spectrometry Accepted Manuscript

Please do not adjust margins

View Article Online
DOI: 10.1039/C6JA00397D

Published on 10 February 2017. Downloaded by University Bordeaux Montaigne on 14/02/2017 11:31:26.

The internal precision (within-spot uncertainty) of all standard analyses averaged 0.06‰. The external precision (spot-to-spot reproducibility) was determined on four grains of the same standard (Gstd0010 with $^{18}\delta O_{true}$= 9.3±0.1‰, 1σ) located in a central position of four different mounts and analyzed several times during the session. Spot-to-spot reproducibility was 0.29-0.5‰ (1σ). Mount-to-mount reproducibility was 0.29‰ (1σ), calculated as the standard deviation of the four Gstd0010 grain averages (Fig. 1a).

The intervals of plagioclase raw $^{18}\delta O$ results obtained from *n* grains casted in different mounts were 5.42-6.82‰ (Gstd0001, An_7, n = 1), 5.81-8.02‰ (Gstd0002, An_6, n = 1), 1.35-4.54‰ (Gstd0003, An_{22}, n = 4), 0.44-4.60‰ (Gstd0004, An_{50}, n = 4), 2.89-3.69‰ (Gstd0005, An_{54}, n = 1), 1.07-2.09‰ (Gstd0006, An_{62}, n = 1), 3.54-5.31‰ (Gstd0008, An_{76}, n = 1) and 2.15-5.78‰ (Gstd0009, An_{96}, n = 2). For K-feldspar, the raw $^{18}\delta O$ intervals were 1.27-5.87‰ (Gstd0010, Or_{89}, n = 6) and 1.43-7.12‰ (Gstd0011, Or_{93}, n = 4). For quartz (Gstd0011, n = 6), the raw $^{18}\delta O$ interval was -2.98 to 3.20‰ (Fig. 1b, c, d).

Most of the plagioclase, K-feldspar, and quartz standards recorded a wide interval of raw $^{18}\delta O$ values, induced by the positional X-Y effect, as the standards were placed in central and also in extreme external positions of the mounts (Fig. 1e), and the variability of electrostatic deflectors (LT1DefX-LT1DefY) values used in the different grains of each standard. The micron-scale compositional and isotopic heterogeneities typical of natural feldspars, even in apparently homogeneous grains, probably also accounted for a small part of these wide ranges of SIMS $^{18}\delta O$ raw results obtained in the standards analyses (see electronic supplementary information S2)†.

After the $^{18}O/^{16}O$ SIMS measurements, the compositions of the craters were constrained by EPMA (included in the electronic supplementary information S2)†. The EPMA analyses were placed around the SIMS spots guided by the BSE images provided by the electron microscope attached to the EPMA. The chemical composition assigned to each SIMS point was determined as the mean of several surrounding EPMA analyses or, as the value obtained in the EPMA nearest neighbour point.

3.5 IMF calculation

The IMF of each SIMS analysis was calculated as the SIMS $^{18}O/^{16}O$ ratio over the reference fluorination $^{18}O/^{16}O$ ratio of the bulk specimen, by Eq. (9):

$$IMF = \frac{^{18}O/^{16}O_{SIMS}}{^{18}O/^{16}O_{fluor}} \quad (9)$$

Expanding (9), IMF can also be expressed in ‰, as Eq. (10):

$$IMF\ (‰) = \left(\frac{^{18}O/^{16}O_{SIMS}}{^{18}O/^{16}O_{fluor}} - 1\right) \times 10^3 \quad (10)$$

The IMF values reported in this study were calculated by equation (9) and, if necessary, expressed in ‰ using equation (10). The approximation of IMF by the expression $IMF\ (‰) \sim (^{18}\delta O_{SIMS} - {}^{18}\delta O_{real})$ was avoided.

The plagioclase IMF values recorded in the center of the mount (i.e. within a 5-6 mm radius) were of the same order than previous plagioclase standards analyzed also using the Cameca 1280HR at the CRPG by Borisova *et al.*[45] These plagioclase IMF averages were -13.8±0.4‰ (1σ) for Gstd0001 (An_7), -14.6±0.5‰ for Gstd0003 (An_{22}), -13.6±0.3‰ for Gstd0005 (An_{54}) and, -12.46±0.5‰ for Gstd0008 (An_{76}).

The complete ranges of IMF went from 0.98312 (-16.88‰) to 0.99055 (-9.45‰) for plagioclase (Fig. 2a), 0.98223 (-17.77) to 0.98790 (-12.1) for K-feldspar (Fig. 2b) and, 0.97804 (-21.96‰) to 0.98432 (-15.68‰) for quartz (Fig. 2c).

The IMF values of all the SIMS analyses are included in the electronic supplementary information S2†.

4 Results of response surface models for IMF prediction

The response surface models of plagioclase, K-feldspar, and quartz were fitted to reach a high predictive power. This approach generated three markedly different models displaying high prediction accuracy. The models were built using the tools of Design of Experiments (DOE) and Response Surface included in the statistical software Minitab 17 (Minitab Inc.). The instructions for fitting a response surface model are included in the electronic supplementary information S4†.

The instrumental input variables included in the three models were the X and Y position, the LT1DefX and LT1DefY electrostatic deflectors values, the chamber pressure (CP), and the primary-ion beam intensity (PI). In addition, the plagioclase model included the compositional input variable anorthite content (An%), and the K-feldspar model, the orthoclase (Or%), and barium (BaO%) contents. The IMF of the SIMS points, calculated by equation (9), was introduced in each model as the response (output variable) to fit. The values of the input variables and the calculated IMF of each SIMS analysis are included in the electronic supplementary information S2†. The selection of the final terms of each model was manually carried out by a stepwise backward elimination process.

4.1 Plagioclase model

The plagioclase model was properly fitted by a second order polynomial including seven linear, three squared and five interactions terms. The complete model design and predictions are included in the electronic supplementary information S3 and S4†. The model equation in the real values of the input variables was Eq. (11):

$$\begin{aligned} IMF_{Plagioclase} = {} & 0.98306 + 1.280E\text{-}7\ X + 2.300E\text{-}6\ Y - \\ & 3.624E{+}5\ CP + 7.000E{+}5\ PI - 1.08E\text{-}5\ LT1defX - \\ & 1.826E\text{-}5\ LT1defY + 3.180E\text{-}5\ An + 3.136E\text{-}11\ X^2 \\ & + 4.083E\text{-}7\ LT1defX^2 + 3.220E\text{-}7\ LT1defY^2 - 4.912E\text{-} \\ & 9\ X{\times}An - 4.250E{+}2\ Y{\times}PI + 3.840E\text{-}9\ Y{\times}An + 2.090E\text{-} \\ & 7\ LT1defX{\times}LT1defY - 3.906E\text{-}7\ LT1LT1defX{\times}An \end{aligned} \quad (11)$$

The ANOVA test indicated that the whole model (F = 65.22), the linear (F = 64.64), interaction (F = 76.11) and the squared

This journal is © The Royal Society of Chemistry 20xx

Please do not adjust margins

Journal of Analytical Atomic Spectrometry Accepted Manuscript

View Article Online
DOI: 10.1039/C6JA00397D

Published on 10 February 2017. Downloaded by University Autonoma de Barcelona on 14/02/2017 11:31:26.

(F = 51.38) parts were significant (Electronic Supplementary Information S3)†. To keep a hierarchical structure, the non-significant terms Y, LT1defY and PI were retained in the model. The multicollinearity of the final terms was low, as the VIF values ranged from 1.94 of X' to 6.50 of (Y × An). The model properly fitted the observations, since R^2 and adjusted-R^2 took 90.47 and 89.09%, respectively. The predictive power was high, as PRESS and prediction-R^2 were 0.0000288 and 86.74%, respectively. The model got a proper discrimination capacity since the adequate precision (A.P.) was 46.6.

The standardized residuals of the model predictions followed a normal distribution (Fig. 3a, c). The plots of standardized residuals vs. fitted IMF (Fig. 3b) and time series (Fig. 3d) showed random distributions, indicating that the most significant variables were included in the model.

Severe influential observations were not detected during the backward elimination process of the model terms. The leverage and Cook's distance of the model points averaged 0.1344±0.0685 and 0.01187±0.02300 (1σ), respectively. Only the SIMS analysis *Pattern2_AN@8* showed high leverage (0.5547), but its Cook's distance was small (0.1718), so it was kept in the model.

The fitted model was right centered on the operational region of the input variables. A Monte Carlo simulation (n = 10^5) of the plagioclase IMF using the fitted model displayed a Gaussian distribution properly aligned with the actual distribution of IMF (Fig. 4), supporting that the fitted model was properly working in the space of the input parameters.

The model took a good predictive capacity, as the scatterplot of the predicted vs. the actual IMF fell on a 1:1 slope (Fig. 5). The absolute difference between the actual and the predicted IMF (/actual IMF-predicted IMF/) averaged 0.000325 ±0.000263 (1σ). In addition, the corrected $\delta^{18}O‰$ results reduced the range of values versus the raw SIMS $\delta^{18}O‰$ in most of the standards. These reductions went from 4.41 to 1.73‰ (61%) in Gstd0003, from 4.15 to 1.63‰ (61%) in Gstd0004, from 1.02 to 0.75‰ (26%) in Gstd0006, from 1.77 to 0.96‰ (46%) in Gstd0008 and from 3.63 to 1.52‰ (58%) in Gstd0009. In Gstd0002, amplitude kept almost constant, from 2.20 to 2.19‰. Only in Gstd0001 and Gstd0005 variability slightly increased, from 1.40 to 1.53‰ (9%) and from 0.80 to 0.94‰ (17%) respectively (Fig. 6). Obviously, the standard values corrected using the model predictions matched the fluorination reference values (Fig. 6). Therefore, the 95% confidence intervals of the model-corrected and the fluorination values intersected the 89% (Gstd0001), 67% (Gstd0002), 75% (Gstd0003), 90% (Gstd0004), 100% (Gstd0005), 100% (Gstd0006), 87% (Gstd0008) and 89% (Gstd0009) of the analyses (Fig. 6a-h).

4.2 K-feldspar model

The K-feldspar model was adequately fitted by a second order polynomial including eight linear, two squared and four interactions terms. The complete model design and predictions can be found in the electronic supplementary information S3 and S4†. The model equation in natural units of the predictor variables was Eq. (12):

$$IMF_{K\text{-}felds} = 1.1170 + 1.340E\text{-}7\ X - 4.590E\text{-}7\ Y - 1.649E{+}7CP - 2.406E{+}7\ PI + 3.100E\text{-}5\ LT1defX - 4.760E\text{-}4\ LT1defY + 1.100E\text{-}6\ Or + 1.598E\text{-}4\ BaO + 1.952E\text{-}11X^2 - 1.207E{+}10\ CP^2 + 5.821E{+}1\ Y{\times}CP + 3.112E{+}15\ CP{\times}PI + 8.190E{+}4\ PI{\times}LT1defY - 1.882E\text{-}6\ LT1defY{\times}BaO \quad (12)$$

The ANOVA results showed that the whole model (*F = 42.73*), linear (*F = 48.76*), interaction (*F = 32.19*), and squared (*F = 33.26*) parts were significant (Electronic Supplementary Information S3)†. To preserve the model hierarchy, the non-significant terms Y, CP, PI, and Or were forced to stay in the model. Multi-collinearity was low, as VIF values went from 1.55 of X^2 to 7.45 of Y. The model reached a good explanatory capacity, since the coefficients R^2 and adjusted-R^2 were 87.56% and 85.51%, respectively. The model presented a proper predictive power, as PRESS and prediction-R^2 were 0.0000234 and 83.17%, respectively. A large signal/noise ratio was obtained since adequate precision (A.P.) was 22.68.

Properly, the standardized residuals displayed Gaussian distribution (Fig. 7a, c). The plots of the residuals vs. fitted IMF (Fig.7b) and time series (Fig. 7d) presented suitable unsystematic distributions.

During the backward elimination process, the SIMS analysis *CHR10_FK1@46* was deleted from the model, as the leverage and Cook's distance presented high values (0.580316 and 0.420016, respectively). This severe influence was probably generated by an extremely high orthoclase content ($Or_{96.7}$). The final model included 101 SIMS points with suitable low influence, as the leverage and Cook's distance averaged 0.1500 ±0.05247 and 0.01085±0.01633 (1σ), respectively.

The Gaussian distributions of the actual and Monte Carlo-simulated (n = 10^5) IMF values were properly aligned (Fig. 8), supporting that the model was correctly centered on the operational region of the predictor variables.

The model reached a suitable predictive capacity, as the scatter plots of the predicted vs. the real IMF followed a 1:1 slope (Fig. 9a). The absolute difference among real and predicted IMF averaged 0.000324±0.000261 (1σ). The model-corrected $\delta^{18}O‰$ results reduced the range of values versus the raw SIMS $\delta^{18}O‰$ from 4.6 to 2.26‰ (51%) for Gstd0010 and from 5.69 to 1.84‰ (68%) for Gstd0011 (Fig. 9b, c). The 95% confidence intervals of the standards corrected values intercepted the 95% confidence intervals of the fluorination results in the 73% (Gstd0010) and 94% (Gstd0011) of the points (Fig. 9b, c), indicating a high predictive accuracy.

4.3 Quartz model

The quartz model was properly fitted by a non-linear polynomial including six linear and one interaction term. The complete model design and the predictions are included in the electronic supplementary information S3 and S4†. The model equation in natural units of the input variables was Eq. (13):

$$IMF_{quartz} = 0.95924 + 2.320E\text{-}7X - 1.570E\text{-}7Y - 7.200E{+}4CP + 4.005{+}6PI - 1.441E\text{-}5LT1defX + 7.906E\text{-}4LT1defY - 1.335E{+}5PI \times LT1defY \quad (13)$$

Journal of Analytical Atomic Spectrometry Accepted Manuscript

Please do not adjust margins

View Article Online
DOI: 10.1039/C6JA00397D

Published on 10 February 2017. Downloaded by Universitat Politecnica de Catalunya on 14/02/2017 11:31:26.

The ANOVA test indicated that the whole model (F = 77.86), the linear (F = 52.74) and the interaction (F = 88.15) parts were significant (Electronic supplementary information S3)†. The non-significant term LT1defY was preserved in the structure to keep a hierarchical polynomial. Multi-collinearity was kept down, as VIF values ranged from 1.58 of PI × LT1defY to 10.01 of X. The determination coefficients R^2 and adjusted-R^2 reached suitable values of 94.29 and 93.08%, respectively. The model obtained a high predictive power, as PRESS and prediction-R^2 were 0.0000094 and 91.59%, respectively. The discrimination capacity was good since adequate precision (A.P.) was 32.87.

The standardized residuals of the model predictions presented a normal-cumulated distribution (Fig. 10a, c). In addition, the plots of residuals vs. fitted IMF values (Fig. 10b) and time series (Fig. 10d) showed adequate random distributions.

During the backward elimination process of the model terms, the SIMS analyses *CHR10_Q@124-123-122-121*-120 were sequentially deleted in this order, as their corresponding pairs of leverage and Cook's distances values were 0.994-3.087, 0.781-0.005, 0.802-0.013, 0.883-1.561, and 0.918-1.674, respectively. Probably, the reason for this severe influence was a large shift of the chamber pressure (Fig. 11). The final model included 42 quartz analyses with adequate influence, since leverage and Cook's distance averaged 0.195±0.070 and 0.026±0.045 (1σ), respectively.

The Gaussian distributions of actual IMF and Monte Carlo simulation ($n = 10^5$) were almost aligned, indicating that the quartz model covered the operational space of the predictor variables (Fig. 12).

The model achieved a strong predictive accuracy, as the scatterplot of the predicted vs. the real IMF fell on a 1:1 slope (Fig. 13a). The averaged absolute difference between the real and predicted IMF was 0.000290±0.000270 (1σ). The model-corrected $\delta^{18}O$‰ results reduced the range of values versus the raw SIMS $\delta^{18}O$‰ from 6.18 to 1.70‰, a decrease of the 72% (Fig. 13b). The model-corrected values were properly situated on the real quartz fluorination value, since the 95% confidence intervals of the model-corrected and the bulk fluorination value intersected in the 97% of the points (Fig. 13b).

5 Discussion

5.1 Insights in the input variables

The coupled examination of the exploratory data analysis (EDA) and the final response surface models of plagioclase, K-feldspar and quartz revealed systematic meaningful trends of IMF vs. the input variables.

5.1.1 X and Y mount location. Notably, IMF systematically presented stronger variation vs. the X-position, showing negative parabolic trends towards the external parts of the mounts and maximums around the zero X-value (Fig. 14a, b). In addition, similar negative parabolic trends of IMF vs. the X-position were also obtained in the response surface models built up using the previously published SIMS data of Śliwiński *et al.* on dolomite-ankerite and Pollington *et al.* on quartz (Fig. 14c, d), both using a Cameca 1280HR (WiscSims).[15,46] Unexpectedly, the variations observed along Y were slightly negative parabolic or linear with low slopes in all the cases, indicating that the variation of IMF along X is much stronger than along Y. In addition, this behaviour is independent of the value ranges of X, Y, and IMF (Fig. 14a, b, c, d). This suggests that at least for the Cameca 1280HR, a close relationship exists between the X position and the instrumental mass bias. As can be observed on the material surface after the SIMS analyses, the incident primary ion-beam of this ion microprobe model excavates half-ellipsoidal craters almost aligned on the X direction. Verdeil *et al.* showed that the ellipsoid of sputtered material elongates in the same direction of the oblique primary-ion beam.[47] Considering this fact, most of the sputtered matter would follow the X direction, and this direction would become significantly more sensitive to IMF than the perpendicular Y direction. In the studies of Kita *et al.,* Treble *et al.*, and Tang *et al.* this close relationship of IMF with the X direction can be also observed.[9,48,49]

5.1.2 LT1defX-LT1defY electrostatic deflectors. Peres *et al.* showed the exponential increase of the electrostatic deflectors values moving beyond 5mm from the center to external X-Y positions using a "normal" sample holder.[50] In consistency with this fact, the electrostatic deflectors values played a major role regarding the IMF prediction by RSM. Systematic positive trends of IMF vs. the electrostatic deflectors (i.e. reduction of IMF) were observed for plagioclase, K-feldspar, and quartz (Fig. 15a, b, c). Notably, this characteristic behaviour of IMF vs. the electrostatic deflectors was also observed in the response surface models fitted using the previously published SIMS data of Śliwiński *et al.*[15] on dolomite-ankerite and Pollington *et al.* on quartz (Fig. 15d, e).[15,46] In all these cases, the IMF variations are stronger along the LT1DefX (or equivalent) than along the LT1DefY (or equivalent), supporting that most of the beam distortion occurs in the X direction. This evolution of IMF vs. the pair of electrostatic deflectors is independent of the value ranges of IMF and the deflectors, highlighting the close dependence of the instrumental mass bias on the action of the electrostatic deflectors. This fact is consistent with the proper centering of the secondary beam achieved with the adequate position of the electrostatic deflectors as has been highlighted by Schuhmacher *et al*.[51]

For a given unknown sample placed far away from the standard, or even in a different mount, the electrostatic deflectors values of both groups of analyses can easily present significant differences. The introduction of the electrostatic deflectors values within the response surface models takes into account these variations. In case it is desired to construct a response surface model using observations resulting from several mounts, it could be helpful to adjust the Z-focus of each mount in a similar X and Y mount position. For this, one possibility is to include a standard specimen located in the same X and Y position to adjust the Z-focusing for all mounts used in a given SIMS session.

5.1.3 Chamber pressure. The inclusion of the chamber pressure in the model was initially unexpected, as most of the

This journal is © The Royal Society of Chemistry 20xx

Journal of Analytical Atomic Spectrometry Accepted Manuscript

View Article Online
DOI: 10.1039/C6JA00397D

Published on 10 February 2017. Downloaded by Universitat Politecnica de Catalunya on 14/02/2017 11:31:26.

SIMS analyses were carried out at ultra-high vacuum conditions (10^{-9}Torr), which can be considered as stable vacuum conditions in a practical sense. However, Outlaw showed that an important increase of residual gas phases occurs during the decrease of the vacuum conditions from $2x10^{-9}$Torr to $2x10^{-7}$Torr.[52] The same author reported a significant increment of the residual gas even in small vacuum leakages from 1.5 to $2.5x10^{-9}$Torr. In ion etching experiments on silicon, Chen *et al.* reported a positive correlation between the excavation of more isotropic etches and the increase of the vacuum values.[20] These observations would support the fact that even small oscillations within the usual range of 10^{-9}Torr vacuum pressure of the Cameca IMS 1280HR could induce an observable mass fractionation. In consistency with this discussion, during this study, the vacuum pressure of five quartz analyses went down to 10^{-8}Torr (4 points) and 10^{-7}Torr (1 point). The respective averaged IMF of these two groups of analyses differ by ~1‰ (10^{-8}Torr points) and ~2‰ (10^{-7}Torr point) with respect to the averaged IMF displayed by the previous five quartz analyses made on the same grain at suitable 10^{-9}Torr pressure conditions (see electronic supplementary information S2)†.

5.1.4 Primary-ion beam intensity. The primary-ion beam intensity showed an unanticipated role over the IMF prediction, as the recorded variations of the primary intensity during the SIMS session were of pico-ampere (10^{-12}A) magnitude. The primary intensity ranged from 5.51 to 6.26 nA (oscillations of 0.75 nA = 750 pA) in plagioclase, from 5.59 to 6.19 nA (0.60 nA = 600 pA range) in K-feldspar and from 5.61 to 6.33 nA (0.72 nA= 720 pA variation) in quartz analyses. Although these pico-ampere oscillations can be considered small, significant effects on the ion excavation process have been reported due to pico-ampere variations of the primary current. For example, Prenitzer *et al.* showed visible changes (using SEM) in the shape of the excavated spots and higher amounts of redeposited material at primary intensities of 500, 1000, and 2000 pico-amperes in Ga^+ ion milling experiments on silicon.[53] From these observations and from the significance of the primary-ion beam obtained in the models, the possibility that the pico-ampere oscillations of the primary ion current at usual operating conditions of the Cameca 1280HR could induce a detectable IMF seems plausible. This effect could be even more evident in the SIMS analyses carried out using pico-ampere primary currents, e.g. the primary ion beams below 20 pA used in small diameter beams (Page *et al.*) or the ~1 pA primary currents used at the NanoSIMS (Hoppe *et al.*).[9,54,55]

5.1.5 Compositional variables. The compositional variables played significantly different roles in the K-feldspar and plagioclase models. For the K-feldspar model, the orthoclase content (Or%) showed low influence over the prediction of IMF. The narrow compositional range of K-feldspar used in this study could account for this reduced effect. However, a second option could be that the composition of alkali feldspars has low significance on IMF, as suggested by the difference about ~0.6‰ among the averaged IMF of albite and K-feldspar specimen, the end-members of the alkali feldspar solid solution series. In agreement with this observation, Ferry *et al.* reported no significant compositional effect in the range orthoclase 75-100%, with an average IMF difference among the Amelia albite and two K-feldspar standards about ~0.6‰, the same magnitude observed in this study.[56]

Unexpectedly, the presence of barium presented a significant role in the K-feldspar model. The high capacity of barium to interact with oxygen would support the hypothesis that small percentages of barium (0-2%) could have a perceptible effect on IMF.[57,58] However, as the barium effect was obtained from two separated populations of IMF values, it should be checked with further experimental work. The exploration of IMF along the orthoclase-celsian (barium feldspars) solid solution series would permit a better exploration of the barium role.

As expected, the anorthite content played a major role in the plagioclase model. The variation magnitude of the averaged IMF vs. An% content was about ~3.5‰ from An_{100} to An_0 (Fig. 16a), in agreement with previous linear regressions fitted by Eiler *et al.*, Coogan *et al.*, Kita *et al.*, Ferry *et al.*, Winpenny & Maclennan and Borisova *et al.*[5,45,56,59–61] Despite these previous work and our study that clearly state the correlation of IMF vs. anorthite content for plagioclase, special care should be taken during the prediction of IMF using only the linear regression of averaged IMF vs. the anorthite content of the standards. The excecution of six separate Monte Carlo simulations ($n = 10^5$) of the main compositional intervals of the plagioclase series, using in each time the complete range of the instrumental variables of this study, showed that these different plagioclase compositions can share a broad range of IMF values (Fig. 16b) due to the instrumental influence. These simulations (Fig. 16b) strongly suggested that the linear regression of the averaged clusters of IMF vs. the averaged plagioclase compositions should be carefully applied during IMF corrections.

5.2 Estimation of the uncertainty

The uncertainty of the response surface predictions showed in this study included two main sources of variability: (1) The variance presented by the *n* fluorination determinations of each standard and (2) the single standard error associated with each prediction of the response surface models. The internal error of each analysis (reproducibility) was not considered a significant source of uncertainty since in all observations it was one order of magnitude lower than the response surface prediction error.

The standard error of the *n* fluorination analyses (σ_{fluor}) of each standard (see Table 1) was considered as the uncertainty associated to the bulk material. The magnitude of this standard error depends on a number of *n* analyses of each standard and on the isotopic homogeneity of the standard crystals.

The standard error of the model predictions (σ_{pred}) of each point *i* was calculated as the uncertainty generated by the response surface models. This standard error of the prediction depends on the *goodness of fit* of the model in the region of the predicted point. Therefore, for a given point $i = 1,2,\dots,n$, the total uncertainty $U_{t,i}$ can be calculated as the combined

Journal of Analytical Atomic Spectrometry Accepted Manuscript

Please do not adjust margins

View Article Online
DOI: 10.1039/C6JA00397D

Published on 10 February 2017. Downloaded by University Bordeaux Montaigne on 14/02/2017 11:31:26.

uncertainty of the corresponding fluorination $\sigma_{fluor,i}$ and prediction $\sigma_{pred,i}$ uncertainties by Eq. (14):

$$U_{t,i} = \sqrt{{\sigma_{fluor,i}}^2 + {\sigma_{pred,i}}^2} \quad (14)$$

Thus, by equation (14), the combined uncertainties averaged 0.23±0.05 (1σ), 0.24±0.05 and 0.32±0.02‰ for plagioclase, K-feldspar, and quartz points respectively.

Equation (14) is able to predict the uncertainty for IMF predicted in the standard measures but the problem consists in the translation of this combined uncertainty to the analyses of samples where the "true" fluorination value is unknown. To estimate the magnitude of this uncertainty, IMF was calculated again for each point *i* by including in the denominator the reference fluorination values $^{18}O/^{16}O_{fluor}$ of each specimen plus their corresponding standard error σ_{fluor} (see Table 1), by Eq. (15):

$$IMF_{u,i} = \frac{^{18}\mathrm{O}/^{16}\mathrm{O}_{\mathrm{SIMS,\,i}}}{^{18}\mathrm{O}/^{16}\mathrm{O}_{\mathrm{fluor}} + \sigma_{\mathrm{fluor}}} \quad (15)$$

This $IMF_{u,i}$ was used as the new output variable to build up three additional response surface models called RS_u for plagioclase, K-feldspar, and quartz, by forcing each new model to include, respectively, the same model terms as the principal response surface models showed before in this study (see electronic supplementary information S3)†. The two response surface models available for each mineral delimited a "sandwich" separated at each point by the difference among both IMF and IMF_u predictions. The total uncertainty $U_{t,i}, i = 1,2,\ldots,n$ was calculated as the maximum possible difference between both predictions, i.e. the maximum thickness of the "sandwich" for each point *i*, by Eq. (16):

$$U_{t,i} = \sqrt{\left(\left(\delta^{18}O_{RSm,i} + \sigma_{RSm,i}\right) - \left(\delta^{18}O_{RSa,i} - \sigma_{RSa,i}\right)\right)^2} \quad (16)$$

Being $\delta^{18}O_{RSm,i}$ and $\sigma_{RSm,i}$ (in ‰ VSMOW) the corrected isotope deviations and their corresponding standard error using the main models of this study and, $\delta^{18}O_{RSa,i}$ and $\sigma_{RSa,i}$ the corrected isotope deviations using the additional response surface predictions and their associated standard errors, respectively.

The total uncertainties (in ‰ VSMOW) calculated by Eq. (16) averaged 0.48±0.10, 0.52±0.20, and 0.64±0.07‰ (1σ) for plagioclase, K-feldspar and quartz, respectively (see electronic supplementary information S3)†. Despite these averaged values that are about double than values calculated by Eq. (14), this method has the advantage, to allow the estimation of the total uncertainty in analyses of unknown samples. Additionally, this method further approximates the uncertainty of the whole isotopic analytical process, involving the initial $^{18}\delta O_{VSMOW}$ fluorination determinations of the standards and the IMF corrections of the SIMS results.

5.3 Design of the sample mounts

To obtain confident IMF predictions of analyses from unknown samples by RSM, the range of values of the predictor variables (inputs) obtained from the accompanying standards should enclose the values of the predictor variables obtained from the unknown samples. In routine SIMS sessions, parameters, such as chamber pressure and primary-ion beam intensity, use to slightly differ from the initially defined operational values. In addition, the electrostatic deflectors will be auto-adjusted for each analysis, remaining "out" of the immediate control of the investigator. These variables under partial "control" are the X and Y position and the chemical composition of the standards. Thus, the use of standards properly placed in X-Y positions to display a central composite design (CCD) can be helpful for the fitting of response surfaces models (Fig. 17a). The number of standards placed in each part of the design would depend on: (i) the number of different mineral species to analyze or (ii) the compositional range covered for a given solid solution series. The CCD design permits a better fitting of expected second order terms of the polynomial, at least for the X and Y positions. However, this type of design requires a larger number of analyses, so it could be excessively material (standards) and time-consuming. Alternatively, the standards could be placed on the X-Y positions following a 2^2 factorial design with central points (Fig. 17b) or a 2^2 factorial design (Fig. 17c). A practical solution in SIMS sessions to fit a second order polynomial could be e.g., the alternated use of mounts with standards placed in CCD and 2^2 factorial designs. To properly constrain the regression coefficients and the residuals of a given response surface model, it would be desirable to obtain at least 10-20 analyses for each variable expected to participate in the model.[62]

5.4 Example of application of RSM to IMF prediction

The three response surface models of this study were applied to the IMF correction of the SIMS $^{18}O/^{16}O$ analyses carried out on plagioclase, K-feldspar, and quartz crystals from several granites samples originating from the Hercynian basement of the Eastern Pyrenees and the Catalan Coastal Ranges, NE Spain.[63] The model-corrected $\delta^{18}O_{VSMOW}$ values of the Ca-bearing plagioclase (7-9‰), the Na-rich plagioclase (10-12‰), and K-feldspar (10-14‰) were in agreement with the $\delta^{18}O$ order of plutonic feldspars $^{18}\delta O_{albite} \approx {}^{18}\delta O_{K\text{-}feldspar} > {}^{18}O\delta_{anorthite}$ and situated the whole rock $^{18}\delta O_{VSMOW}$ of the granites within the range of High $\delta^{18}O$ magmas.[64] The quartz results presented a bimodal distribution, with one group situated at 9-12‰ and a second one displaying significant lower values of 6-8‰.

To compare with the corrections achieved by RSM, the IMF of several analyses of the granite samples were also calculated applying the usual method of the bracketing standards for each subset of points. For the plagioclase, the response surface corrected $\delta^{18}O_{VSMOW}$ results went from 6.99 to 9.28‰, whereas the bracket corrected values ranged from 8.58 to 10.85‰ (Fig. 18). The differences point-by-point oscillated from -0.77 to -1.60‰, with an average of -1.28±0.30‰ (1σ) and an absolute average difference of 1.28±0.30‰ (1σ). For the K-feldspar, the response surface corrected $\delta^{18}O_{VSMOW}$ values went from 10.42 to 13.81‰, while the bracket corrections took from 9.66 to 14.22‰ (Fig. 18). Point-by-point, the difference went from -0.95 to +2.33‰, with an average

This journal is © The Royal Society of Chemistry 20xx

Please do not adjust margins

Journal of Analytical Atomic Spectrometry Accepted Manuscript

View Article Online
DOI: 10.1039/C6JA00397D

Published on 10 February 2017. Downloaded by Universitat Politecnica de Catalunya on 14/02/2017 11:31:26.

difference of 0.67±0.89‰ (1σ) and an absolute average difference of 0.90±0.64‰ (1σ). For the quartz, the response surface corrected $\delta^{18}O_{VSMOW}$ values ranged from 6.39 to 11.89‰, whereas the bracket corrections went from 5.85 to 10.97‰ (Fig. 18). The quartz differences reach from -1.66 to +3.23‰, with an average difference of 0.41±1.44‰ (1σ) and an absolute average difference of 1.23±0.82‰ (1σ). Despite the averaged differences among the two correction methods could seem rather small, both procedures gave significantly different corrections for most of the compared analyses (Fig. 18).

The standardization of these differences (dividing by the standard deviation) presents a positive trend versus the combined standardized differences among the samples and the standards values of the LT1DefX and LT1DefY deflectors and of the radial position (Fig. 19a). Thus, when the sample and the standard are close from each other and display similar deflector values, the results are similar, independently of the used correction method (Fig. 19a). In Figure 19b the case of two K-feldspar analyses is represented. The b.1-pair is located very close, showing similar X-Y deflector and radial location values, in this case, the correction using any of the two methods arises to similar values. In contrast, the b.2-pair corresponds to a sample analysis with the standard used for bracket correction located in a different radial location of the mount and with different LT1DefX-LT1DefY values. Therefore, the correction of the b.2 sample analysis by the bracket method or by the RSM method gives very different results (Fig. 19a).

Figure 19c shows two plagioclase analyses; in this case, c.1 and c.2-pairs have similar distances between the sample and the standard (used for bracket correction) but the radial location of every pair is very different and accounts for differences observed in the Y-axis (Fig. 19a). Thus, the difference between both correction methods is lower for the c.1-pair.

Finally, Figure 19d shows two pairs with the typical relation also observed in Figure 19b (d.1 and d.2-pairs). However, the sample analysis and the standard of the d.3 pair have very different radial location inside the mount and LT1DefX and LT1DefY deflectors values too, but the RSM and the bracket correction arise to similar values. In this particular case, the "personalized" IMF given by the RSM function has the same value than the real IMF calculated for the standard used in the bracket correction but it can be considered as a coincidence. In fact, all the quartz analyses with Y-axis < 1 and high X-axis values correspond to analyses performed in the same mount and under the same conditions (Fig. 19a). This effect can also account for the high dispersion observed in the graph of Figure 19a.

The observed differences between the response surface and bracket corrected results could lead to significantly varying conclusions in the studies of micro-textural features e.g. zoned grains, reaction rims, grain overgrowths, micro-crack fillings or intragrain diffusion, where each single SIMS result becomes important by itself.

6 Conclusions

The results of this study showed that RSM can be confidently applied to IMF prediction in stable isotope SIMS analyses by using instrumental and compositional variables. Importantly, the proper predictions of IMF are achieved when the range of values of the variables from the unknown analyses (i.e. the samples to correct) are situated within the range of values of the standards used to fit the model (i.e. RSM predicts by interpolation). It is not recommended to extrapolate the predictions beyond the operational region of the variables.

The models showed that IMF prediction is strongly dominated by the instrumental parameters, in particular the X and Y positions and the electrostatic deflectors values. The chamber pressure and the primary-ion beam intensity are also significant for IMF prediction in most of the cases but are not too critical if their oscillations within a session remain one order of magnitude below the defined working conditions.

Concerning the compositional parameters, the anorthite content is essential for plagioclase IMF prediction, while orthoclase content has a smaller influence on K-feldspar IMF prediction, at least in the orthoclase extreme member of the alkali feldspars solid solution series. The barium content pointed to a potential role in IMF prediction of K-feldspar but needs to be confirmed by further experiments. Notably, quartz IMF can be adequately predicted by the only use of instrumental variables. These results confirm that RSM is effective for IMF correction in solid solution series and in individual minerals.

From a qualitative vision, obtaining satisfactory SIMS results requires a large economic and time-consuming effort (i.e. samples and standards preparation, pre-SIMS SEM-EDS, CL and EPMA analyses, SIMS session, post-SIMS EPMA analyses, data processing, IMF calculation…). Importantly, RSM provides a new powerful IMF-correction method that complements the traditional standard-bracketing method, and, as the most significant variables affecting IMF can be simultaneously screened, permits SIMS researchers to improve the control and confidence on their IMF corrections. Likewise, RSM has proven to be useful dealing with situations where one or several subsets of results obtained from the bracketing-standards used for correction are not satisfactory enough. Furthermore, RSM could be applied to the SIMS analysis of large mm-scale polycrystalline rock fragments, where the standards and the unknown sample analyses could present important differences in values of X-Y positions and electrostatic deflectors. Likewise, RSM can also be used for the design of experiments (DOE) to explore the IMF behavior under determinate instrumental and compositional conditions. Although IMF-correction by RSM appears to be a complex and time-consuming task, fitting RSM models using adequate statistical software requires a relatively short and straightforward learning. Using good quality SIMS data, a trained researcher can fit a useful RSM model in several hours, even faster than the normal data processing for standard-bracketing correction.

Journal of Analytical Atomic Spectrometry Accepted Manuscript

This journal is © The Royal Society of Chemistry 20xx

Please do not adjust margins

View Article Online
DOI: 10.1039/C6JA00397D

Published on 10 February 2017. Downloaded by Universitat Politècnica de Catalunya on 14/02/2017 11:31:26.

Further experimental work could expand the prediction of IMF by RSM to other isotopes, mineral phases, and types of ion microprobes. In addition, data mining and machine learning techniques like, e.g. artificial neural networks (ANN) could improve the fitting and improving IMF prediction models in stable isotope SIMS analyses.

Acknowledgements

We thank two anonymous reviewers who significantly contributed to enhance this paper. We also want to thank members of the CRPG Ion Probe Group for discussion and comments during the internal seminar dedicated the application of RSM to IMF correction. This is CRPG contribution number 2483. Thanks to the technical staff of the Laboratorio General de Análisis de Isótopos Estables of the Universidad de Salamanca (Nucleus), especially the laboratory chief Clemente Recio, for the fluorination analyses and his technical comments. Xavier Llobet (Serveis Científico Tècnics of the Universitat de Barcelona) for his technical assistance in the EPMA analyses. Joaquim Sanz (Museum of Geology Valentí Masachs, Escola Politècnica Superior d'Enginyeria of Manresa) for his help in acquiring suitable standard specimens. Pura Alfonso (Escola Politècnica Superior d'Enginyeria of Manresa) for her comments about the characteristics of feldspars and quartz. Albert Fàbrega for his mathematical comments and corrections. Galit Shmueli (Institute of Service Science, National Tsing Hua University, Taiwan) for her useful comments about the predictive and explanatory power of statistical models. This research was performed within the framework of DIHIME Project (CGL2015-66355-C2-1-R of DGICYT, Ministerio de Economia y Competitividad, Gobierno de España) and Grup Consolidat de Recerca "Geologia Sedimentària" (2014-SGR-251), Control, Dynamics and Applications (CoDAlab) (2014-SGR-859) and Grup de Recerca en Mineria Sostenible (2014-SGR-1069) supported by the Comissionat per a Universitats i Recerca del Departament d'Empresa i Coneixement de la Generalitat de Catalunya.

References

1 L. R. Riciputi, B. A. Paterson and R. L. Ripperdan, *Int. J. Mass Spectrom.*, 1998, **178**, 81–112, DOI: 10.1016/s1387-3806(98)14088-5.
2 V. R. Deline, C. A. Evans and P. Williams, *Appl. Phys. Lett.*, 1978, **33**, 578, DOI: 10.1063/1.90466.
3 N. Shimizu and S. R. Hart, *Annu. Rev. Earth Planet. Sci.*, 1982, **10**, 483–526, DOI: 10.1146/annurev.ea.10.050182.002411.
4 E. Hauri, J. Wang, J. E. Dixon, P. L. King, C. Mandeville and S. Newman, *Chem. Geol.*, 2002, **183**, 99–114, DOI: 10.1016/s0009-2541(01)00375-8.
5 J. M. Eiler, C. Graham and J. W. Valley, *Chem. Geol.*, 1997, **138**, 221–244, DOI: 10.1016/s0009-2541(97)00015-6.
6 A. A. Gurenko, M. Chaussidon and H.-U. Schmincke, *Geochim. Cosmochim. Acta*, 2001, **65**, 4359–4374, DOI: 10.1016/s0016-7037(01)00737-2.
7 E. Hauri, A. Shaw, J. Wang, J. Dixon, P. King and C. Mandeville, *Chem. Geol.*, 2006, **235**, 352–365, DOI: 10.1016/j.chemgeo.2006.08.010.
8 D. Vielzeuf, M. Champenois, J. Valley, F. Brunet and J. Devidal, *Chem. Geol.*, 2005, **223**, 208–226, DOI: 10.1016/j.chemgeo.2005.07.008.
9 N. T. Kita, T. Ushikubo, B. Fu and J. W. Valley, *Chem. Geol.*, 2009, **264**, 43–57, DOI: 10.1016/j.chemgeo.2009.02.012.
10 F. Z. Page, N. T. Kita and J. W. Valley, *Chem. Geol.*, 2010, **270**, 9–19, DOI: 10.1016/j.chemgeo.2009.11.001.
11 C. Rollion-Bard and J. Marin-Carbonne, *J. Anal. At. Spectrom.*, 2011, **26**, 1285–1289, DOI: 10.1039/c0ja00213e.
12 M. E. Hartley, T. Thordarson, C. Taylor, J. G. Fitton and EIMF, *Chem. Geol.*, 2012, **334**, 312–323, DOI: 10.1016/j.chemgeo.2012.10.027.
13 G. Slodzian, C. Engrand and J. Duprat, *Nucl. Instruments Methods Phys. Res. Sect. B Beam Interact. with Mater. Atoms*, 2012, **275**, 41–57, DOI: 10.1016/j.nimb.2011.12.019.
14 R. B. Ickert and R. a. Stern, *Geostand. Geoanalytical Res.*, 2013, **37**, 429–448, DOI: 10.1111/j.1751-908x.2013.00222.x.
15 M. G. Śliwiński, K. Kitajima, R. Kozdon, M. J. Spicuzza, J. H. Fournelle, A. Denny and J. W. Valley, *Geostand. Geoanalytical Res.*, 2016, **40**, 157–172, DOI: 10.1111/j.1751-908x.2015.00364.x.
16 M. G. Śliwiński, K. Kitajima, R. Kozdon, M. J. Spicuzza, J. H. Fournelle, A. Denny and J. W. Valley, *Geostand. Geoanalytical Res.*, 2016, **40**, 173–184, DOI: 10.1111/j.1751-908x.2015.00380.x.
17 G. E. P. Box and K. B. Wilson, *J. R. Stat. Soc. Ser. B*, 1951, **13**, 1–45.
18 P. E. Riley, *J. Electrochem. Soc.*, 1989, **136**, 1112, DOI: 10.1149/1.2096795.
19 R. Legtenberg, *J. Electrochem. Soc.*, 1995, **142**, 2020, DOI: 10.1149/1.2044234.
20 K.-S. Chen, A. A. Ayon, X. Zhang and S. M. Spearing, *J. Microelectromechanical Syst.*, 2002, **11**, 264–275, DOI: 10.1109/jmems.2002.1007405.
21 C. C. Hung, H. C. Lin and H. C. Shih, *Solid. State. Electron.*, 2002, **46**, 791–795, DOI: 10.1016/s0038-1101(02)00004-7.
22 H. Angellier, L. Choisnard, S. Molina-Boisseau, P. Ozil and A. Dufresne, *Biomacromolecules*, 2004, **5**, 1545–1551, DOI: 10.1021/bm049914u.
23 M. Y. Noordin, V. C. Venkatesh, S. Sharif, S. Elting and A. Abdullah, *J. Mater. Process. Technol.*, 2004, **145**, 46–58, DOI: 10.1016/s0924-0136(03)00861-6.
24 D. Baş and İ. H. Boyacı, *J. Food Eng.*, 2007, **78**, 836–845, DOI: 10.1016/j.jfoodeng.2005.11.024.
25 M. A. Bezerra, R. E. Santelli, E. P. Oliveira, L. S. Villar and L. A. Escaleira, *Talanta*, 2008, **76**, 965–977, DOI: 10.1016/j.talanta.2008.05.019.
26 S. S. Habib, *Appl. Math. Model.*, 2009, **33**, 4397–4407, DOI: 10.1016/j.apm.2009.03.021.
27 C. R. T. Tarley, G. Silveira, W. N. L. dos Santos, G. D. Matos, E. G. P. da Silva, M. A. Bezerra, M. Miró and S. L. C. Ferreira, *Microchem. J.*, 2009, **92**, 58–67, DOI: 10.1016/j.microc.2009.02.002.
28 K. Ali, S. A. Khan and M. Z. M. Jafri, *Superlattices Microstruct.*, 2012, **52**, 782–792, DOI: 10.1016/j.spmi.2012.06.008.
29 A. W. Azhari, K. Sopian, M. K. M. Desa and S. H. Zaidi, *Appl. Surf. Sci.*, 2015, **357**, 1863–1877, DOI: 10.1016/j.apsusc.2015.09.088.
30 O. A. Mohamed, S. H. Masood and J. L. Bhowmik, *Appl. Math. Model.*, 2016, in press, DOI: 10.1016/j.apm.2016.06.055.
31 G. E. P. Box, *Biometrics*, 1954, **10**, 16, DOI: 10.2307/3001663.
32 G. E. P. Box and N. R. Draper, *Response Surfaces, Mixtures, and Ridge Analyses*, Wiley-Interscience, 2007.
33 K. M. Carley, N. Y. Kamneva and J. Reminga, *Response Surface Methodology: CASOS Technical Report*, School of

This journal is © The Royal Society of Chemistry 20xx

Journal of Analytical Atomic Spectrometry Accepted Manuscript

Please do not adjust margins

View Article Online
DOI: 10.1039/C6JA00397D

Computer Science, Carnegie-Mellon University, Pittsburgh, Pittsburgh, US, 2004.
34 E. del Castillo, *Process Optimization. A statistical approach*, Springer US, Boston, MA, US, 2007, vol. 105.
35 R. H. Myers, D. C. Montgomery and C. M. Anderson-Cook, *Response Surface Methodology. Process and Product Optimization Using Designed Experiments*, John Wiley & Sons, Inc., New York, NY, US, 2009.
36 A. I. Khuri and S. Mukhopadhyay, *Wiley Interdiscip. Rev. Comput. Stat.*, 2010, **2**, 128–149, DOI: 10.1002/wics.73.
37 R. R. Barton, in *Encyclopedia of Operations Research and Management Science*, eds. S. I. Gass and M. C. Fu, Springer US, Boston, MA, 2013, pp. 1307–1313.
38 G. Shmueli, *Stat. Sci.*, 2010, **25**, 289–310, DOI: 10.1214/10-sts330.
39 D. L. Dowe, S. Gardner and G. Oppy, *Br. J. Philos. Sci.*, 2007, **58**, 709–754, DOI: 10.1093/bjps/axm033.
40 C. Hitchcock and E. Sober, *Br. J. Philos. Sci.*, 2004, **55**, 1–34, DOI: 10.1093/bjps/55.1.1.
41 S. Konishi and G. Kitagawa, *Information Criteria and Statistical Modeling*, Springer, New York, US, Springer., 2008.
42 G. Shmueli and O. Koppius, *Manag. Inf. Syst. Q.*, 2011, **35**, 553–572.
43 R. D. Cook, in *International Encyclopedia of Statistical Science*, ed. M. Lovric, Springer Berlin Heidelberg, Berlin, Heidelberg, 2011, pp. 301–302.
44 F. W. Witkowski, D. J. Blundell, P. Gutteridge, A. D. Horbury, N. H. Oxtoby and H. Qing, *Mar. Pet. Geol.*, 2000, **17**, 1085–1093, DOI: 10.1016/s0264-8172(00)00055-6.
45 A. Y. Borisova, A. A. Gurenko, C. Martel, K. Kouzmanov, A. Cathala, W. A. Bohrson, I. Pratomo and S. Sumarti, *Geochim. Cosmochim. Acta*, 2016, **190**, 13–34, DOI: 10.1016/j.gca.2016.06.020.
46 A. D. Pollington, R. Kozdon, L. M. Anovitz, R. B. Georg, M. J. Spicuzza and J. W. Valley, *Chem. Geol.*, 2016, **421**, 127–142, DOI: 10.1016/j.chemgeo.2015.11.011.
47 C. Verdeil, T. Wirtz, H.-N. Migeon and H. Scherrer, *Appl. Surf. Sci.*, 2008, **255**, 870–873, DOI: 10.1016/j.apsusc.2008.05.231.
48 P. C. Treble, A. K. Schmitt, R. L. Edwards, K. D. McKeegan, T. M. Harrison, M. Grove, H. Cheng and Y. J. Wang, *Chem. Geol.*, 2007, **238**, 197–212, DOI: 10.1016/j.chemgeo.2006.11.009.
49 G.-Q. Tang, X.-H. Li, Q.-L. Li, Y. Liu, X.-X. Ling and Q.-Z. Yin, *J. Anal. At. Spectrom.*, 2015, **30**, 950–956, DOI: 10.1039/c4ja00458b.
50 P. Peres, N. T. Kita, J. W. Valley, F. Fernandes and M. Schuhmacher, *Surf. Interface Anal.*, 2013, **45**, 553–556, DOI: 10.1002/sia.5061.
51 M. Schuhmacher, F. Fernandes and E. de Chambost, *Appl. Surf. Sci.*, 2004, **231–232**, 878–882, DOI: 10.1016/j.apsusc.2004.03.157.
52 R. A. Outlaw, in *Handbook of Vacuum Science and Technology*, eds. D. M. Hoffman, B. Singh, J. H. Thomas and J. H. Thomas, Academic Press, San Diego, 1998, pp. 335–375.
53 B. I. Prenitzer, C. A. Urbanik-Shannon, L. A. Giannuzzi, S. R. Brown, R. B. Irwin, T. L. Shofner and F. A. Stevie, *Microsc. Microanal.*, 2003, **9**, 216–236, DOI: 10.1017/s1431927603030034.
54 P. Hoppe, S. Cohen and A. Meibom, *Geostand. Geoanalytical Res.*, 2013, **37**, 111–154, DOI: 10.1111/j.1751-908x.2013.00239.x.
55 F. Z. Page, T. Ushikubo, N. T. Kita, L. R. Riciputi and J. W. Valley, *Am. Mineral.*, 2007, **92**, 1772–1775, DOI: 10.2138/am.2007.2697.
56 J. M. Ferry, K. Kitajima, A. Strickland and J. W. Valley, *Geochim. Cosmochim. Acta*, 2014, **144**, 403–433, DOI: 10.1016/j.gca.2014.08.021.
57 E. Ozensoy, C. H. F. Peden and J. Szanyi, *J. Phys. Chem. B*, 2006, **110**, 17001–17008, DOI: 10.1021/jp060668l.
58 E. Ozensoy, C. H. F. Peden and J. Szanyi, *J. Phys. Chem. B*, 2006, **110**, 17009–17014, DOI: 10.1021/jp060669d.
59 L. A. Coogan, C. E. Manning, R. N. Wilson and E.I.M.F, *Earth Planet. Sci. Lett.*, 2007, **260**, 524–536, DOI: 10.1016/j.epsl.2007.06.013.
60 N. T. Kita, T. Ushikubo, B. Fu, M. Spicuzza and J. Valley, *Lunar Planet. Sci.*, 2007, **XXXVIII**, 1–2.
61 B. Winpenny and J. Maclennan, *J. Petrol.*, 2014, **55**, 2537–2566, DOI: 10.1093/petrology/egu066.
62 F. E. Harrell, *Regression Modeling Strategies: With Applications to Linear Models, Logistic and Ordinal Regression, and Survival Analysis*, Springer International Publishing, Cham, Heidelberg, New York, Dordretcht, London, 2015.
63 Carles Fàbrega, D. Parcerisa, D. Gòmez-Gras, A. Travé, C. Franke and A. Gurenko, in *Geoquímica ambiental a Catalunya. Recull d'articles. Monografies tècniques de l'Institut Cartogràfic i Geològic de Catalunya, núm. 5*, eds. M. Vilà, I. Herms and J. Cirés, Institut Cartogràfic i Geològic de Catalunya, Barcelona, Spain, 2016, pp. 83–95.
64 I. Bindeman, A. Gurenko, O. Sigmarsson and M. Chaussidon, *Geochim. Cosmochim. Acta*, 2008, **72**, 4397–4420, DOI: 10.1016/j.gca.2008.06.010.

Published on 10 February 2017. Downloaded by Universitat Politècnica de Catalunya on 14/02/2017 11:31:26.

Journal of Analytical Atomic Spectrometry Accepted Manuscript

Please do not adjust margins

View Article Online
DOI: 10.1039/C6JA00397D

Published on 10 February 2017. Downloaded by Universitat Politecnica de Catalunya on 14/02/2017 11:31:36.

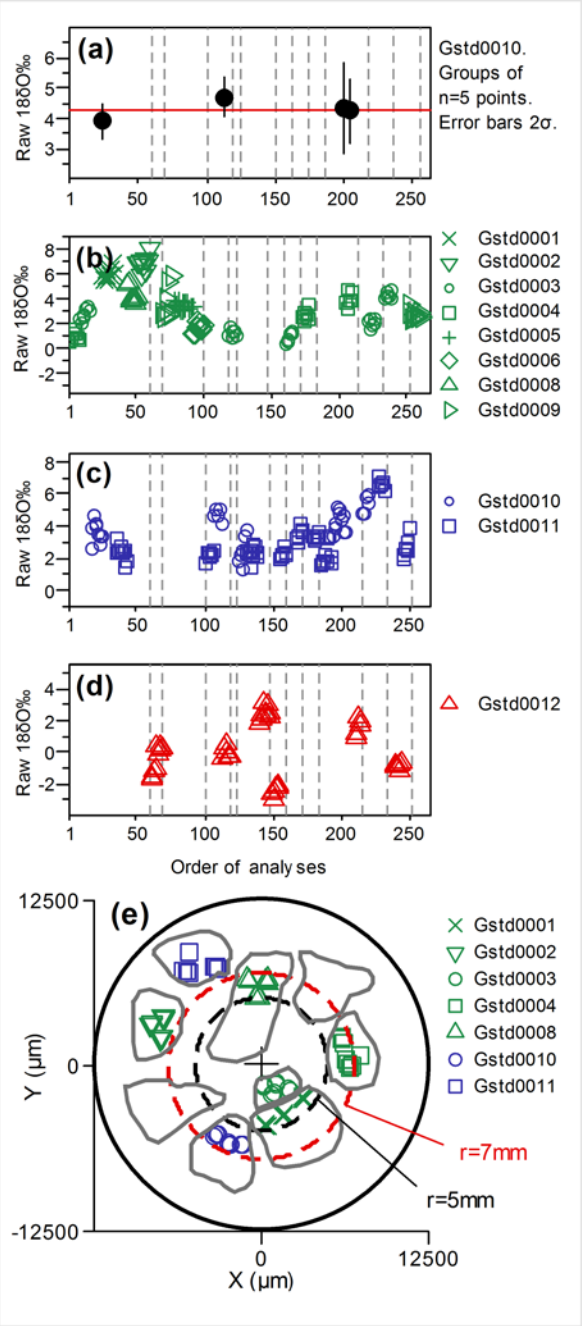

Fig. 1 (a) Mount to mount reproducibility of raw $^{18}\delta O_{VSMOW}$ results was 0.29‰ (1σ), estimated as the standard deviation among four grains of Gstd0010. The internal average of each grain was calculated using five spots. (b, c, d) Time series of the raw $^{18}\delta O_{VSMOW}$ results for plagioclase (b), K-feldspar (c) and quartz (d) analyses. Grey vertical dashed lines indicate the mount changes. (e) Schematic X-Y coordinates of the analyses on plagioclase and K-feldspar standards grains in the representative mount *Pattern1*.

View Article Online
DOI: 10.1039/C6JA00397D

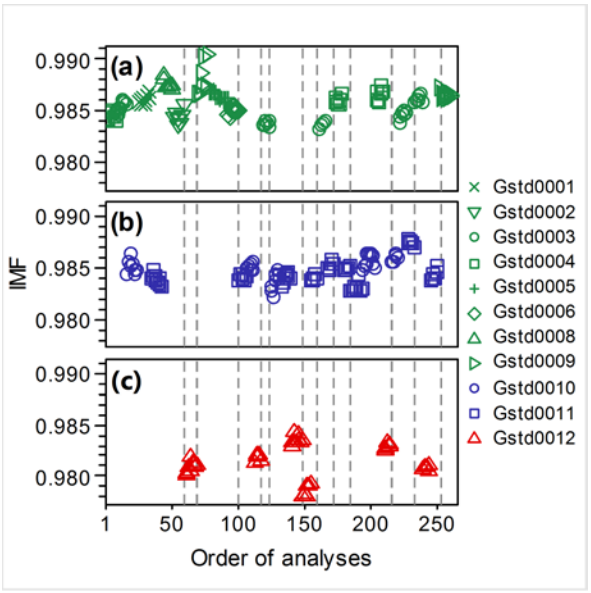

Fig. 2 Time series of the calculated IMF values for plagioclase (a), K-feldspar (b) and quartz (c) analyses. Vertical dashed lines indicate the mount changes.

Published on 10 February 2017. Downloaded by Universitat Politecnica de Catalunya on 14/02/2017 11:31:36.

View Article Online
DOI: 10.1039/C6JA00397D

Figure 3

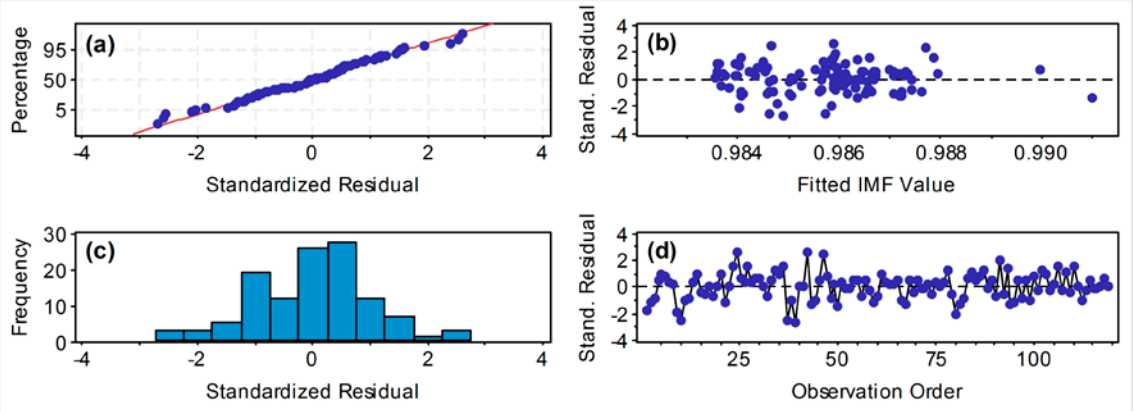

Fig. 3 Graphs of standardized residuals for the plagioclase model. (a) Cumulative normal probability plot of standardized residuals. (b) Random distribution of standardized residuals vs. fitted IMF values. (c) Histogram of standardized residuals. (d) Random time series of standardized residuals.

Published on 10 February 2017. Downloaded by Universitat Politecnica de Catalunya on 14/02/2017 11:31:36.

View Article Online
DOI: 10.1039/C6JA00397D

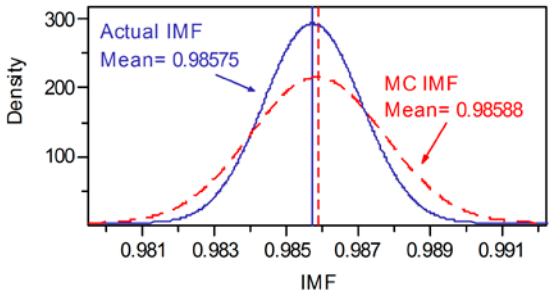

Fig. 4 Plagioclase normal probability plots of the actual (blue) and the Monte Carlo (MC) simulated using the RSM model (red dashed) IMF values. The close alignment of both populations supports that the model is properly centered on the real operational region of the input variables.

Published on 10 February 2017. Downloaded by Universitat Politecnica de Catalunya on 14/02/2017 11:31:36.

View Article Online
DOI: 10.1039/C6JA00397D

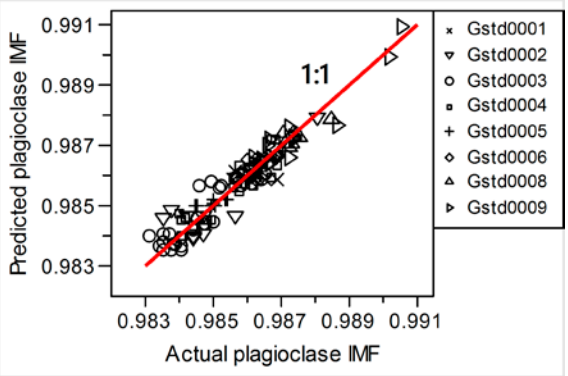

Fig. 5 Scatterplot of the RSM-predicted vs. the actual plagioclase IMF. The points follow a 1:1 slope, supporting the predictive power of the plagioclase model.

Published on 10 February 2017. Downloaded by Universitat Politecnica de Catalunya on 14/02/2017 11:31:36.

View Article Online
DOI: 10.1039/C6JA00397D

Figure 6

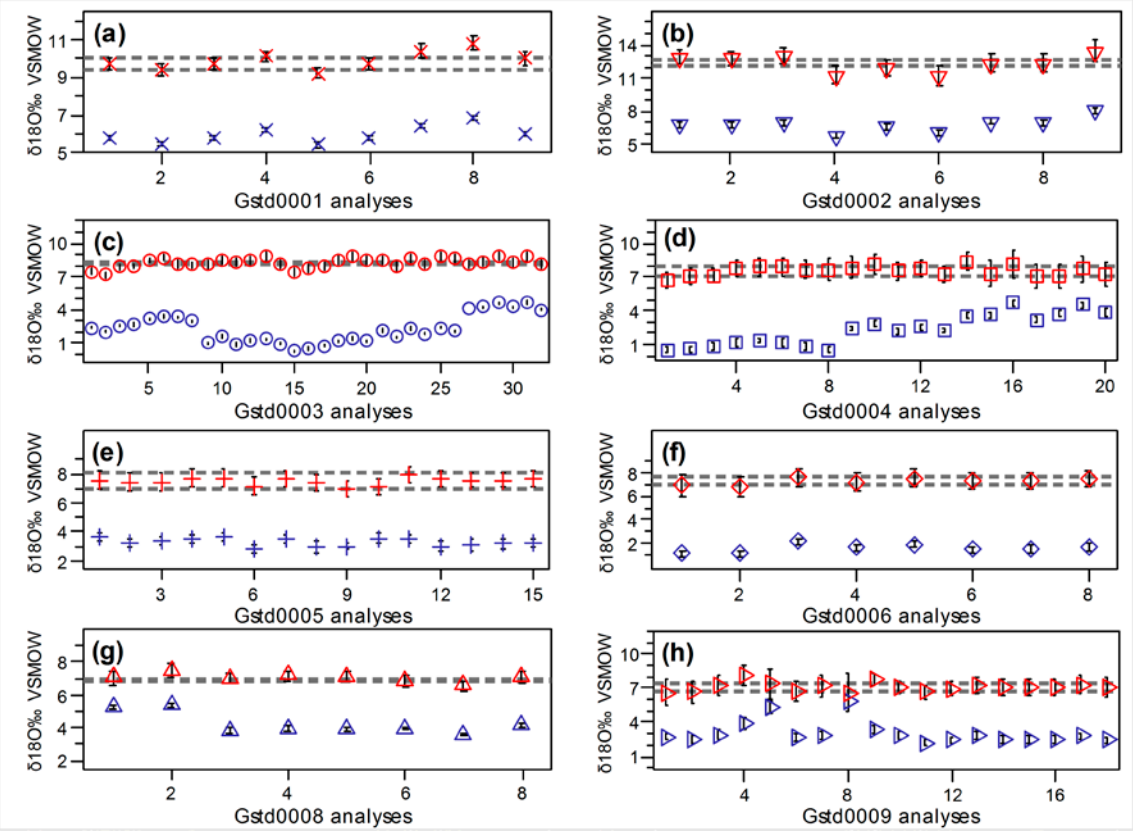

Fig. 6 (a-h) Time series of the plagioclase standards showing the $^{18}\delta O_{VSMOW}$ raw SIMS (blue symbols) and their corresponding RSM-corrected values (red symbols). Error bars are ±2σ. σ represents the internal error of each SIMS point for the raw results and the standard error of the predictions for the RSM-corrected values. The grey horizontal dashed lines delimit the ±2σ interval (95% confidence) of the reference fluorination value of each plagioclase standard. As the set of plagioclase analyses covers all the SIMS session, the plagioclase RSM-model presents valid predictive power for all the session.

Published on 10 February 2017. Downloaded by Universitat Politecnica de Catalunya on 14/02/2017 11:31:36.

View Article Online
DOI: 10.1039/C6JA00397D

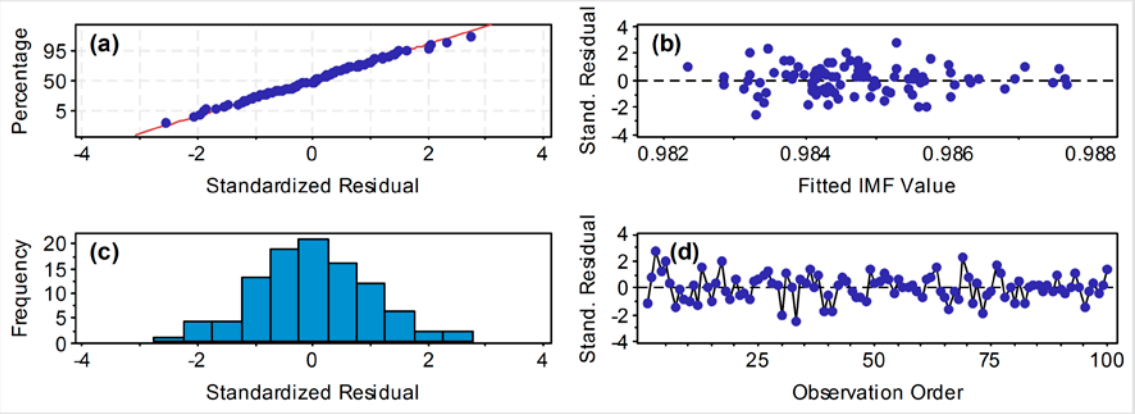

Fig. 7 Plots of standardized residuals for the K-feldspar model. (a) Cumulative normal probability plot of standardized residuals. (b) Randomly distributed standardized residuals vs. fitted IMF values. (c) Normal histogram of standardized residuals. (d) Random time series of standardized residuals.

Published on 10 February 2017. Downloaded by Universitat Politecnica de Catalunya on 14/02/2017 11:31:36.

View Article Online
DOI: 10.1039/C6JA00397D

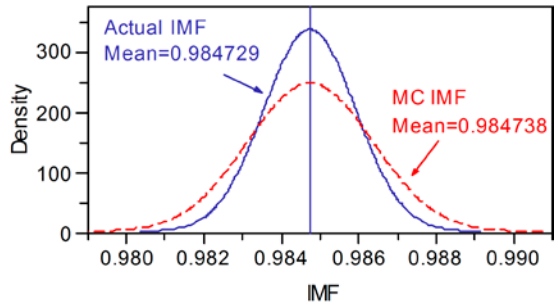

Fig. 8 K-feldspar normal probability plots of the actual (blue) and the Monte Carlo (MC) simulated using the RSM-model (red dashed) IMF values. The good agreement of the two populations supports that the model is situated on the real operational region of the input variables.

Published on 10 February 2017. Downloaded by Universitat Politecnica de Catalunya on 14/02/2017 11:31:36.

View Article Online
DOI: 10.1039/C6JA00397D

Published on 10 February 2017. Downloaded by Universitat Politecnica de Catalunya on 14/02/2017 11:31:36.

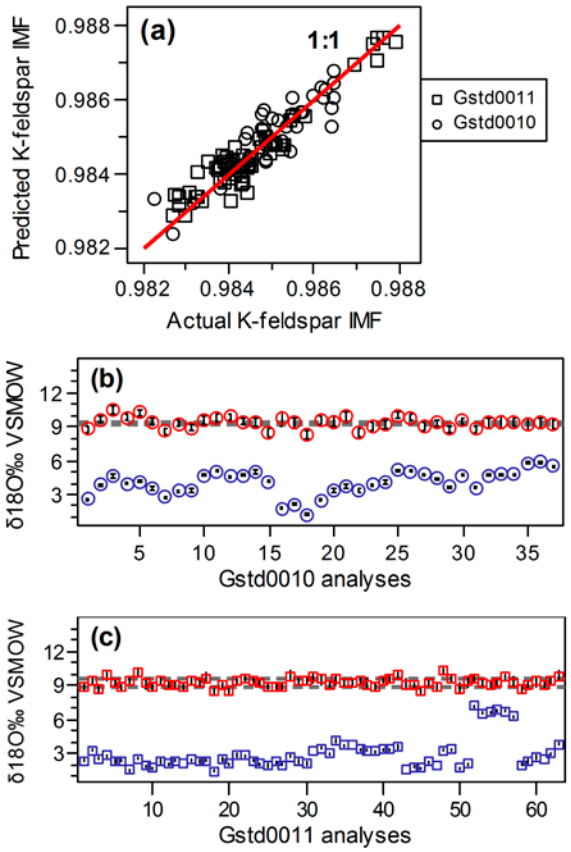

Fig. 9 (a) Scatterplot of the RSM-predicted vs. the actual K-feldspar IMF. The points are scattered along the 1:1 slope, supporting the predictive power of the K-feldspar model. (b, c) Time series of K-feldspar standards showing the $^{18}\delta O_{VSMOW}$ raw SIMS (blue symbols) and their corresponding RSM-corrected value (red symbols). Error bars are ±2σ. σ represents the internal error of each SIMS point for the raw results and the standard error of the predictions for the RSM-corrected values. Grey horizontal dashed lines delimit the ±2σ interval (95% confidence) of the reference fluorination value of each standard. As the sequence of K-feldspar analyses covers the complete SIMS session, the K-feldspar model presents predictive power for the entire session.

Figure 10

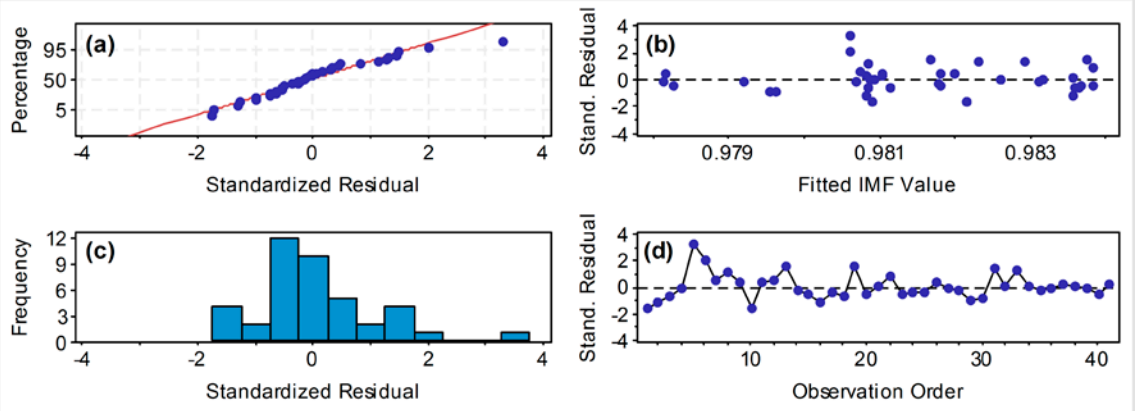

Fig. 10 Standardized residuals of the quartz model. (a) Cumulative normal probability plot of standardized residuals. (b) Random standardized residuals vs. fitted IMF values. (c) Histogram of standardized residuals. (d) Structureless time series of standardized residuals.

Published on 10 February 2017. Downloaded by Universitat Politecnica de Catalunya on 14/02/2017 11:31:36.

View Article Online
DOI: 10.1039/C6JA00397D

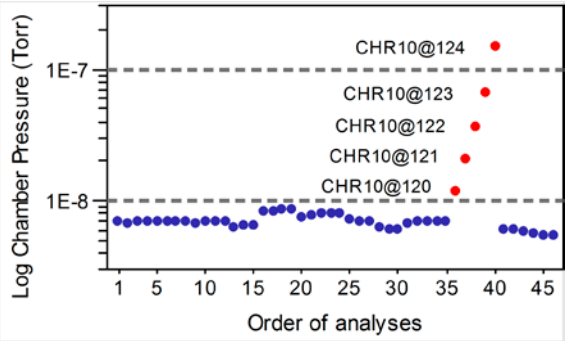

Fig. 11 Quartz chamber pressure values showing a significant vacuum drop during five analyses (red points) of the sample CHR10. These points were deleted during the backward elimination process of the model terms due to their severe influence (high Leverage and Cook's distance values).

Published on 10 February 2017. Downloaded by Universitat Politecnica de Catalunya on 14/02/2017 11:31:36.

View Article Online
DOI: 10.1039/C6JA00397D

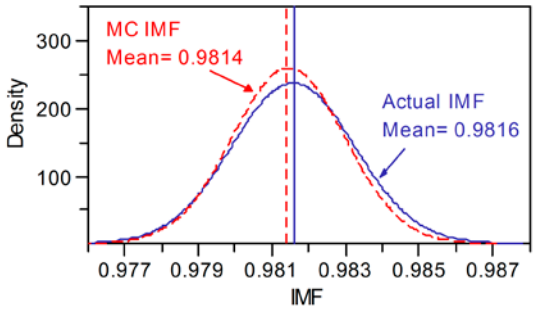

Fig. 12 Quartz normal probability plots of the actual (blue) and the Monte Carlo (MC) simulated using the RSM-model (red dashed) IMF values. The good adjustment of both distributions supports that the quartz model was situated on the real operational region of the input variables.

Published on 10 February 2017. Downloaded by Universitat Politecnica de Catalunya on 14/02/2017 11:31:36.

View Article Online
DOI: 10.1039/C6JA00397D

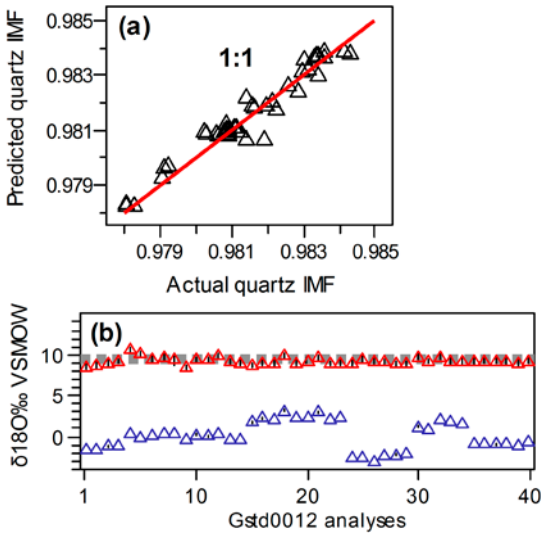

Fig. 13 (a) Scatterplot of the RSM-predicted vs. the actual quartz IMF. The points follow a 1:1 slope, supporting the predictive capability of the quartz model. (b) Time series of quartz showing the $^{18}\delta O_{VSMOW}$ raw SIMS (blue triangles) and the RSM-corrected (red triangles) values. Error bars are ±2σ. σ represents the internal error of each SIMS point for the raw results and the standard error of the predictions for the RSM-corrected values. The grey horizontal dashed lines indicate the ±2σ interval (95% confidence) of the reference fluorination value of quartz. Importantly, as the whole set of quartz analyses covers all the SIMS session, the quartz model presents predictive power for the complete session.

Published on 10 February 2017. Downloaded by Universitat Politecnica de Catalunya on 14/02/2017 11:31:36.

View Article Online
DOI: 10.1039/C6JA00397D

Published on 10 February 2017. Downloaded by Universitat Politecnica de Catalunya on 14/02/2017 11:31:36.

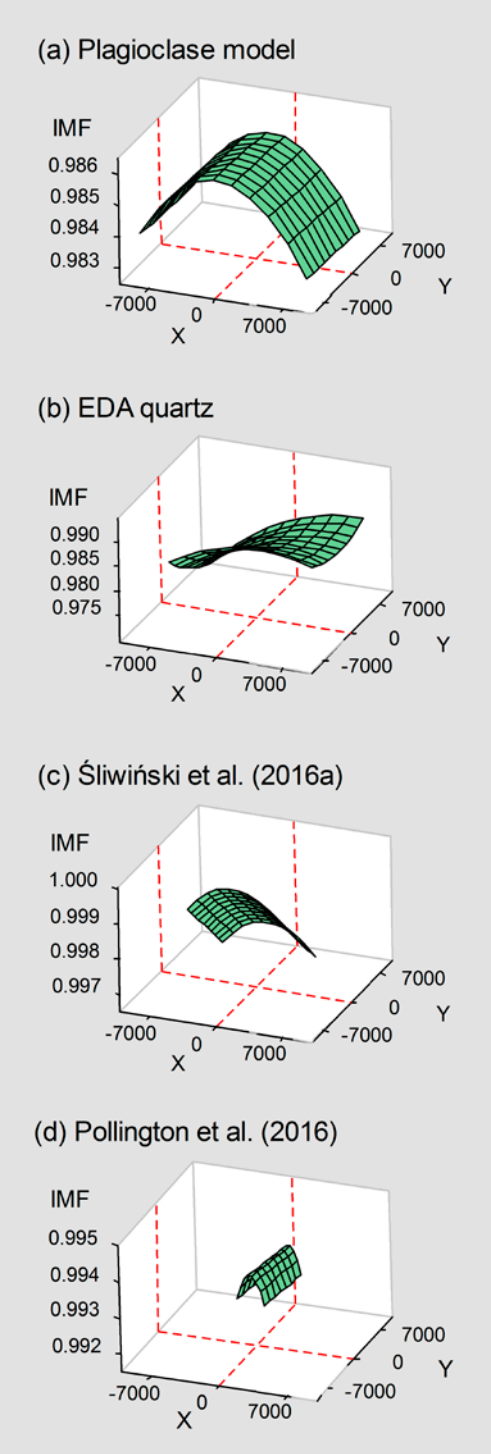

Fig. 14 3D surfaces of IMF vs. X and Y position obtained from: (a) Response surface model of plagioclase. (b) EDA of the quartz data. (c) Response surface model constructed with the published data of Śliwiński *et al.* on dolomite- ankerite.[15] (d) Response surface model built up using the published data of Pollington *et al.* on quartz.[46]

View Article Online
DOI: 10.1039/C6JA00397D

Published on 10 February 2017. Downloaded by Universitat Politecnica de Catalunya on 14/02/2017 11:31:36.

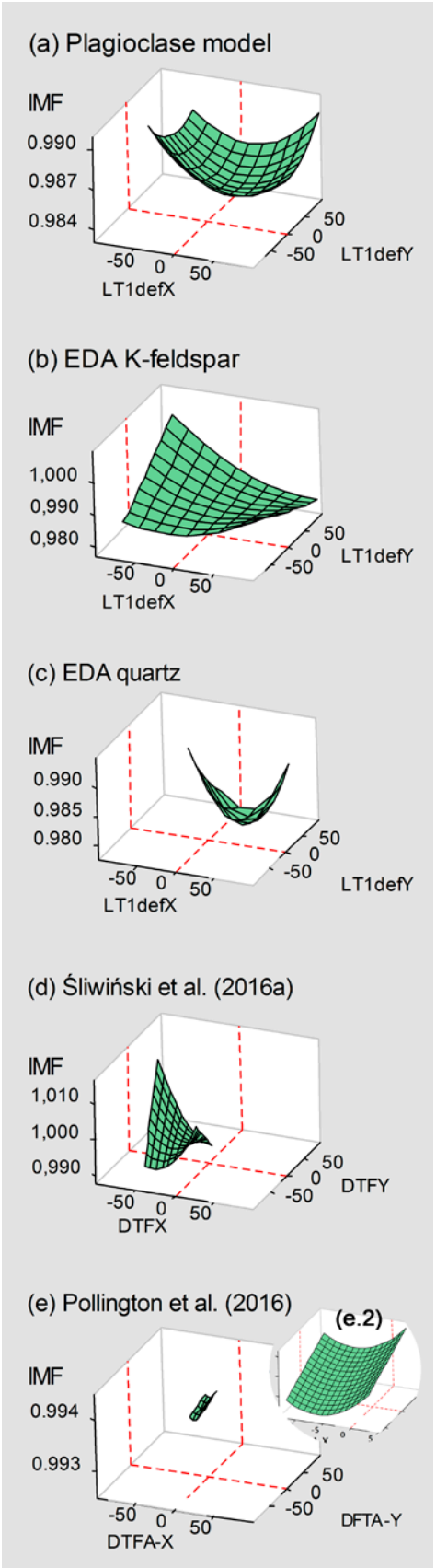

Fig. 15 3D surfaces IMF vs. LT1DefX and LT1DefY (or equivalents ones) obtained from: (a) Plagioclase response surface model. (b) EDA of the K-feldspar data. (c) EDA of the quartz data. (d) Response surface

View Article Online
DOI: 10.1039/C6JA00397D

model constructed using the published data of Śliwiński *et al.* on dolomite-ankerite.[15] (e) Response surface model fitted using the published data of Pollington *et al.* on quartz.[46] (e.2) Zoom of the surface (e).

Published on 10 February 2017. Downloaded by Universitat Politecnica de Catalunya on 14/02/2017 11:31:36.

View Article Online
DOI: 10.1039/C6JA00397D

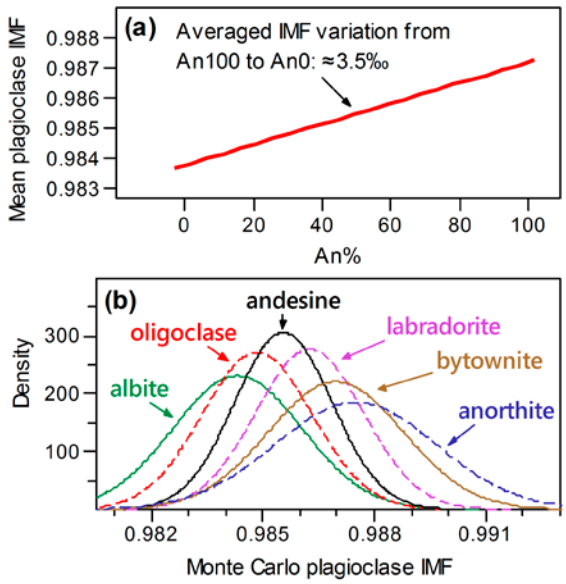

Fig. 16 (a) Main effect plot of mean IMF vs. anorthite content for the plagioclase model. The vertical axis represents the averaged IMF values obtained for any fixed anorthite content applying the real interval of values of the rest of variables. (b) Monte Carlo simulations using the plagioclase RSM-model for the six intervals of plagioclase composition, applying in each of them the real intervals of values of the instrumental variables recorded for the plagioclase analyses of this study. The MC-simulated Gaussian distributions of each standard overlap among them for a wide range of IMF values, highlighting the strong influence of the instrumental variables on IMF.

Published on 10 February 2017. Downloaded by Universitat Politecnica de Catalunya on 14/02/2017 11:31:36.

View Article Online
DOI: 10.1039/C6JA00397D

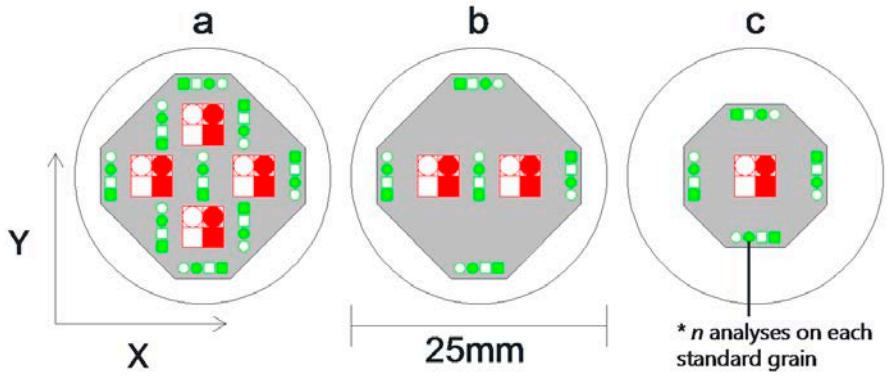

Fig. 17 Schematic X-Y positions for sets of standards (green symbols) and the unknown samples (red symbols) in the mounts, proposed to improve the fitting of response surface models. (a) Position of the standards following a central composite design (CCD), with the potential capacity to generate a response surface model to correct four sample fragments. (b) 2^2 factorial design with central point able to correct two sample fragments. (c) 2^2 factorial design with one sample located in the core of the mount. The grey polygons indicate the area covered by a potential response surface model.

Published on 10 February 2017. Downloaded by Universitat Politecnica de Catalunya on 14/02/2017 11:31:36.

View Article Online
DOI: 10.1039/C6JA00397D

Figure 18

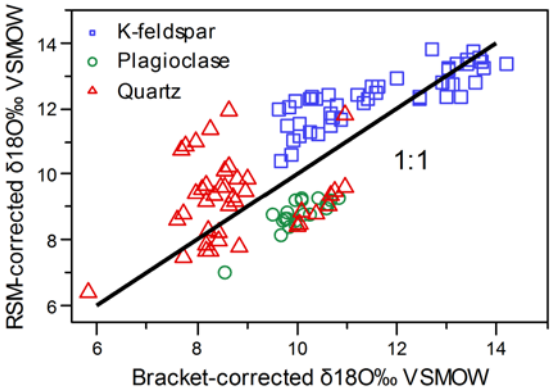

Fig. 18 Scatterplot of the RSM-corrected vs. the bracket-corrected $^{18}\delta O_{VSMOW}$ results. Notably, the three mineral groups display trends that fall away from the 1:1 slope, indicating that for most of the analyses, both methods gave significant different corrections.

Published on 10 February 2017. Downloaded by Universitat Politecnica de Catalunya on 14/02/2017 11:31:36.

View Article Online
DOI: 10.1039/C6JA00397D

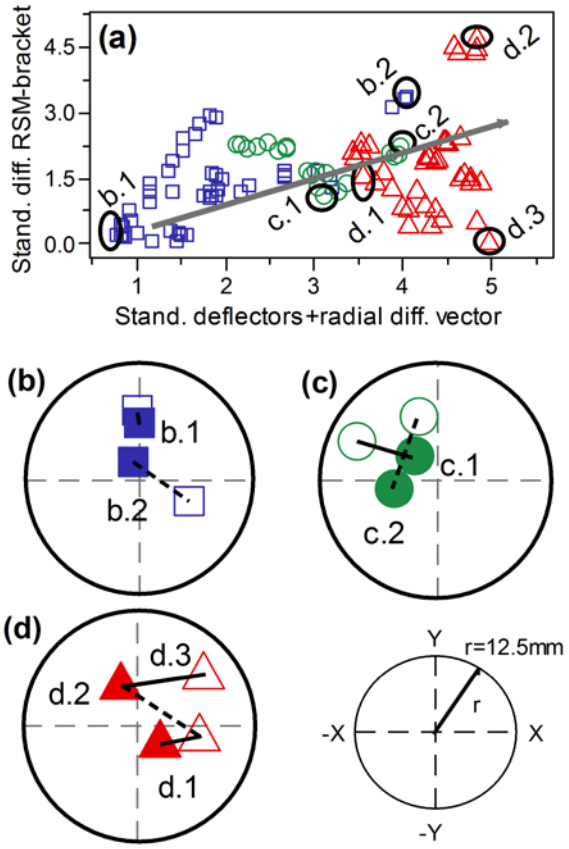

Fig. 19 (a) Standardized absolute difference between the response surface and bracket corrected results vs. the vector of the standardized differences among the standards and the samples for the LT1DefX and LT1DefY deflectors' values and the radial location. (b, c, d) Positions of the samples (full symbols) and the corresponding bracket standards (empty symbols) joined by black lines. Continuous lines indicate situations with low radial position difference, while dashed lines indicate a high difference in the radial position.

Published on 10 February 2017. Downloaded by Universitat Politecnica de Catalunya on 14/02/2017 11:31:36.